A COMBINED NUMERICAL-EXPERIMENTAL INVESTIGATION ON MICRO-EXTRUSION

A THESIS SUBMITTED TO
THE GRADUATE SCHOOL OF NATURAL AND APPLIED SCIENCES
OF
ATILIM UNIVERSITY
BY

LEVENT MURAT

IN THE FULFILLMENT OF THE REQUIREMENTS FOR THE DEGREE OF

MASTER OF SCIENCE

IN THE DEPARTMENT OF MANUFACTURING ENGINEERING

April 2013

Approval of the Graduate School of Natural and Applied Sciences, Atılım University.

_____

Prof. Dr. İbrahim AKMAN

Director

I certify that this thesis satisfies all the requirements as a thesis for the degree of Master of Science.

_____

Prof. Dr. Gülhan ÖZBAYOĞLU

Head of Department

This is to certify that we have read the thesis "A Combined Numerical-Experimental Investigation on Micro Extrusion " submitted by " Levent MURAT " and that in our opinion it is fully adequate, in scope and quality, as a thesis for the degree of Master of Science.

_____ _____

Asst. Prof. Dr. Merih ŞENGÖNÜL — Co-Supervisor

Asst. Prof. Dr. İzzet ÖZDEMİR — Supervisor

Examining Committee Members

Asst. Prof. Dr. İzzet ÖZDEMİR _____

Asst. Prof. Dr. Merih ŞENGÖNÜL _____

Asst. Prof. Dr. Caner ŞİMŞİR _____

Asst. Prof. Dr. Celalettin KARADOĞAN _____

Asst. Prof. Dr. Cihan TEKOĞLU _____

DECLERATION OF AUTHORSHIP

I declare and guarantee that all data, knowledge and information in this document has been obtained, processed and presented in accordance with academic rules and ethical conduct. Based on these rules and conducts, I have fully cited and referenced all materials and results that are not original to this work.

Signed: _____

Date: _____

ABSTRACT

A COMBINED NUMERICAL-EXPERIMENTAL INVESTIGATION ON MICRO-EXTRUSION

BY

LEVENT MURAT

Supervisor:Asst. Prof. Dr. İzzet Özdemir

Co-supervisor:Asst. Prof. Dr. Merih Şengönül

April 2013, 63 pages

In this work, to develop an understanding on micro forming processes, a combined experimental-numerical investigation on micro forming is presented. On the experimental side, in order to demonstrate the statistical size effect, an experimental set-up for micro-extrusion has been designed and micro-extrusion test with copper billets of different average grain size, has been conducted successfully. On the modelling side, due to large displacement and large strains developing during the forming process, a geometrically non-linear continuum mechanics description is preferred. Since a grain level description is necessary for micro forming operations, crystal plasticity is used to model the mechanical response of each grain. To this end, the crystal plasticity framework has been coded as a user defined material model and integrated into the commercial FE software Abaqus as a UMAT subroutine. With this tool, a numerical investigation on the influence of grain orientations on frictional response at small scales is carried out.

Keywords: Micro Forming, Micro Extrusion, Finite Element Method, Crystal Plasticity,Grain Orientation, UMAT Subroutine.

MİKRO-EKSTRÜZYON İŞLEMİ ÜZERİNE DENEYSEL-SAYISAL BİR İNCELEME

Murat Levent

Tez Yöneticisi: Yar. Doç Dr. İzzet Özdemir

Yardımcı Tez Yöneticisi: Yar. Doç Dr. Merih Şengönül

Nisan 2013, 63 sayfa

Bu çalışmada, mikro şekillendirme işlemleri ile ilgili bir anlayış geliştirebilmek için mikro ekstrüzyon üzerine deneysel ve sayısal araştırmaları içeren bir çalışma sunulmaktadır. Deneysel tarafta; istatiktiksel boyut etkisini göstermek için bir dizi mikro ekstrüzyon deney düzeneği hazırlanmış, farklı ortalama tanecik büyüklüklüğüne sahip bakır çubuklar kullanılarak mikro ekstrüzyon testleri başarıyla gerçekleştirilmiştir. Modelleme kısmında ise, şekillendirme boyunca oluşan büyük yerdeğiştirme-büyük gerinimler dikkate alınarak, geometrik olarak lineer olmayan sürekli ortamlar mekaniği tercih edilmiştir. Mikro şekillendirme süreçlerinde tanecik büyüklüğü seviyesinin tanımlanması gerekliliğinden dolayı Kristal Plastisite teorisi mekanik davranışın modellenmesinde kullanılmıştır. Bu amaçla Kristal Plastisite teorisine bağlı kullanıcı tanımlı malzeme modeli kodlanarak Sonlu Elemanlar Analiz Programı "Abaqus" içine entegre edilmiştir. Bu şekilde küçük ölçeklerde tanecik yönelimlerinin sürtünme parametresi üzerine olan etkisi sayısal olarak incelenmiştir.

Anahtar Kelimeler : Mikro şekillendirme, Mikro Ekstrüzyon, Sonlu Elemanlar Metodu, Kristal Plastisite, Tanecik Yönelimleri, UMAT.

ACKNOWLEDGEMENTS

I express sincere appreciation to my supervisor Asst. Prof. Dr. İzzet Özdemir and co-supervisor Asst. Prof. Dr. Merih Şengönül for their guidance and insight throughout the research. I would also like to thank for the support they provided me with all through this study.

TABLE OF CONTENTS

LIST OF FIGURES

LIST OF TABLES

To My Family. . .

CHAPTER 1

INTRODUCTION

The emergence of advanced technologies in many fields such as medical and micro-electronics has produced a significant demand for miniaturized components. Representative samples from different fields can be seen in figure 1.1.

FIGURE 1.1: Examples of micro-components from different fields [1]

Micro-manufacturing is concerned with the techniques, equipments and systems for manufacturing of components that have at least two dimensions in the range of sub-millimeters. In the field of forming at larger scales (conventional engineering scale), extensive amount of experience and theoretical and practical knowledge has accumulated in years. Exploring this inheritance in the context of micro-forming would be a very rational way to achieve cost effective, versatile micro-forming technologies. However, it has turned out that this route is not realizable due to complex material and frictional behaviour at small scales. Therefore, it has became essential to develop a proper understanding about material and interface (friction) behaviour at such small scales, which in turn could be used to develop dedicated processes for the manufacturing of metallic micro-components shown in figure 1.2.

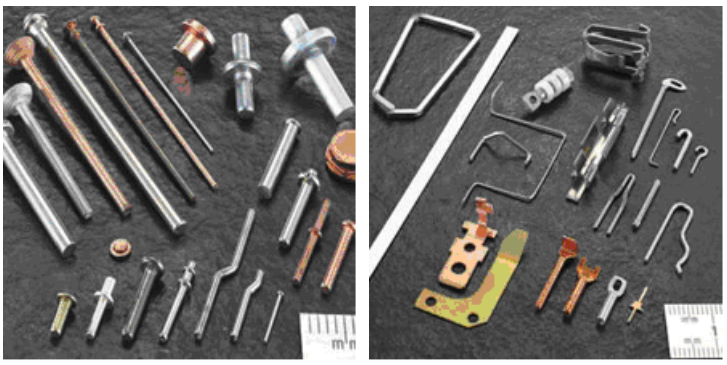

FIGURE 1.2: Representation of metallic micro-components [2]

The complex material and tribological behaviour at small scales is due to the phenomena known as the size effect. As the components size approach to the typical micro-structural size (grain size) upon miniaturization, statistical and physical size effect arises.

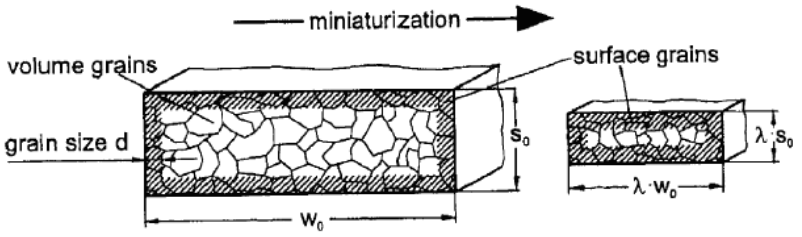

FIGURE 1.3: The relation between the surface and inside grain [3]

As the size of the components gets smaller, the ratio of the number of grains located at the boundaries to the number of grains surrounded by other grains (internal grains) increases. Upon deformation, this implies that hardening mechanism due to dislocation - grain boundary interaction is weakened and dissimilar hardening behaviour is observed for the two samples shown in figure 1.3. Another physical size effect source could be explained by bending experiments on very thin metallic films. Since the plastic strains are non-homogeneous along the thickness, the dislocation densities has to be non-homogeneous as well. The regions where plastic strains are larger have to accommodate extra dislocations (known as geometrically necessary dislocations (GND's)). For films with different thickness, reaching the same level of curvature implies significantly different GND distributions which in turn influences the yielding and hardening behaviour of the sample, as shown in the graph in figure 1.4.

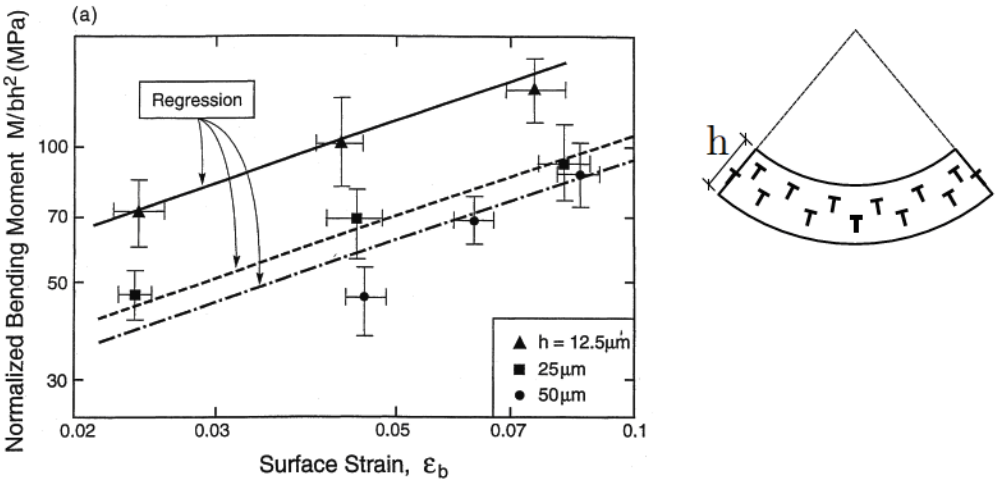

FIGURE 1.4: Representation of the size effect on Metallic thin films which are applied micro-bending test[4].

It is well known that, the micro-structure of a crystalline metal at meso-level is an assembly of grains. Each grain has a lattice orientation which is one of the primary characteristics dictating the mechanical behaviour upon external loading. In case of large components, randomly oriented thousand of grains result in an isotropic behaviour at the component scale. However, since the number of grains is diminishing as the components get smaller, the behaviour of individual grains become more pronounced and decisive on the overall component behaviour. This fact leads to a "statistical" size effect which is reflected in experiments as large scatters and dissimilar physical response as shown in figure 1.5, where micro-extrusion experiments with different grain sizes had been conducted.

High volume of micro-part manufacturing is the target of the micro-forming process at an industrial scale. In the context of mass production, many other factors such as part local features, tolerance and surface quality, material selection issues have to be addressed. Unfortunately the standards on many aspects of these issues have not been established fully yet.

As far as modelling of processes such as micro-extrusion is concerned, it is obvious that conventional modelling approaches based on classical plasticity theories do not reflect the real physical behaviour and far from being predictive.

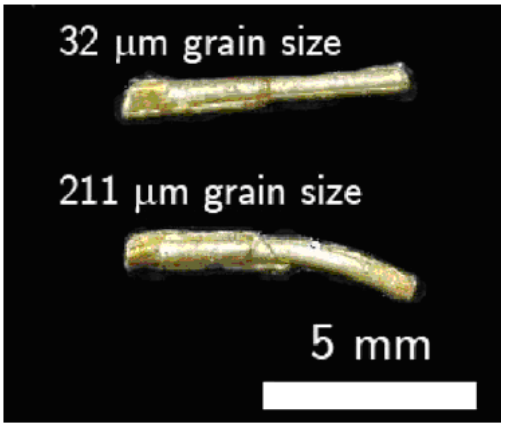

FIGURE 1.5: Curving tendency of extruded micro-pin with different grain size [5]

Motivated by these observations and the challenge in modelling of micro-forming processes, a combined experimental and numerical study on micro-extrusion has been conducted. After a brief literature review given in the next chapter, the experimental set-up designed for micro-extrusion process is detailed in chapter 3 along with the experimental results. Afterwards, the modelling framework, namely the crystal plasticity at large strains is concisely presented and complemented with the resulting finite element solution framework. The following chapter is dedicated to investigate the influence of grain orientation statistics on frictional response during extrusion with the implemented numerical tool. Finally the thesis is closed with conclusions and possible extension of the work in the last chapter.

CHAPTER 2

LITERATURE REVIEW

Starting with the early 90's, there has been a growing body of research output, which is closely tied with the increasing demand on industrial applications. The conducted studies can be classified into four groups such as:

- Studies on physical size effect
- Studies on statistical size effect
- Studies on friction and surface roughness effect at small scales
- Studies on modelling micro-forming processes

A survey on the state of the art in micro-forming can be found in Vollersten et al. [6] Since proper material characterization is the essential step in understanding the overall process, Meisner [3] investigated the effect of miniaturization on flow characteristics of the material by means of upsetting experiments. Test conducted with CuZn15 specimens indicated that the flow curves decreases (shift downward) upon miniaturization.

As briefly mentioned in chapter 1, this tendency is attributed to the fact that the number of grains completely surrounded by other grains is decreasing as compared to the number of grains located on the boundaries of the specimen upon miniaturization. As far as dislocation-grain boundary interaction is concerned, this has an adverse effect on hardening response of the material. Experimental results obtained by the Geiger and Engel [7] confirmed the same tendency. They conducted both tension and upsetting tests on CuZn15 samples and got the characteristics results shown in figure 2.1.

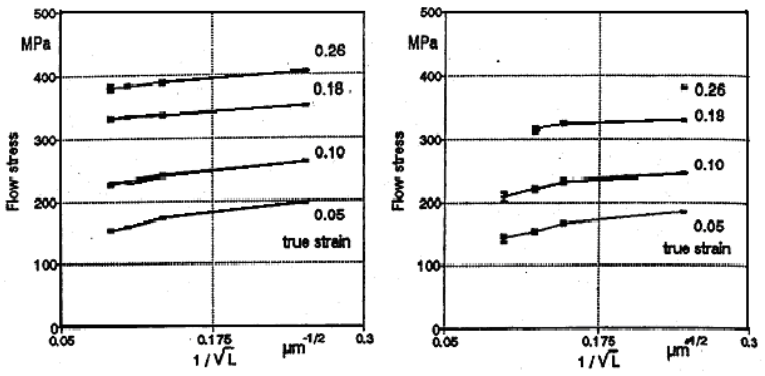

FIGURE 2.1: Flow curves: results of tension tests (at right) and upsetting tests (at left), [7].

In recent extrusion experiments to produce sub-millimetre sized parts [5], the researchers have seen a curving tendency in the extrudate with a random curving direction. Tests on samples of various average grain sizes indicated that, the curving tendency is strongly related with the average grain size, disappearing when the average grain size is sufficiently small as compared to the component size, figure 2.2

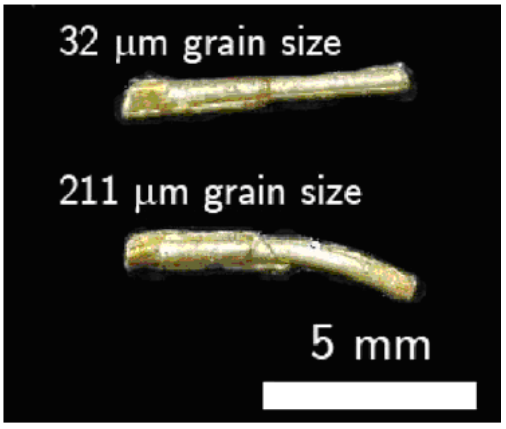

FIGURE 2.2: Curving tendency of extruded micro-pin with different grain size [5]

To investigate the relation between the grain size and friction coefficient, Espinosa et al. [5] conducted dynamic extrusion tests with a Kolksy apparatus. The results showed that there is no statistical effect of grain size on the contact pressure and specimen size on both static and dynamic friction coefficients. However, the reported dynamic friction coefficients lie in the interval of 0.18 and 0.32 [8, 9, 10]. The large scatter

might be explained by the other factors such as grain orientation and surface roughness which were not considered in the study.

In order to investigate the effect of temperature on micro-forming process, Egerer and Engel [11] conducted micro backward can extrusion and upsetting experiments. Due to the tendency of homogenization in flow curve, at elevated temperatures, the scatter in process characteristics, e.g, force-displacement curves decrease. Their study indicates that, in micro forming, the process can be better controlled at elevated temperature. To investigate the effect of component size on friction, Teisler[12] performed experiments using a scaled double cup extrusion set-up as shown in figure 2.3.

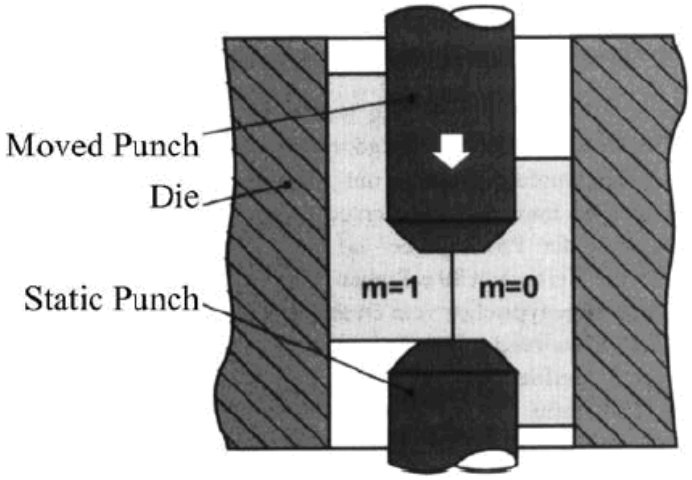

FIGURE 2.3: Metal flow in double cup exrusion test depending on friction [12]

Cylindrical CuZn15 specimens of varying diameter (4.0 mm to 0.5 mm) were used in the lubricated double cup extrusion tests. A very significant increase in friction (up to 20 times) was observed with the decreasing specimen diameter. This size effect in friction is attributed to the so called open and closed lubricant pockets on the surface of the work piece. Due to the surface roughness, see figure 2.4, during extrusion the peaks are flattened and the closed lubricant pockets are created in the valleys. But if the valley is located at the free surfaces(open lubricant pockets), the lubricant can easily escape.

In another study, Cao et al [13] have investigated the micro-extrusion process to manufacture micro-pins of 0.8 mm diameter using 2mm diameter billets and micro-pins

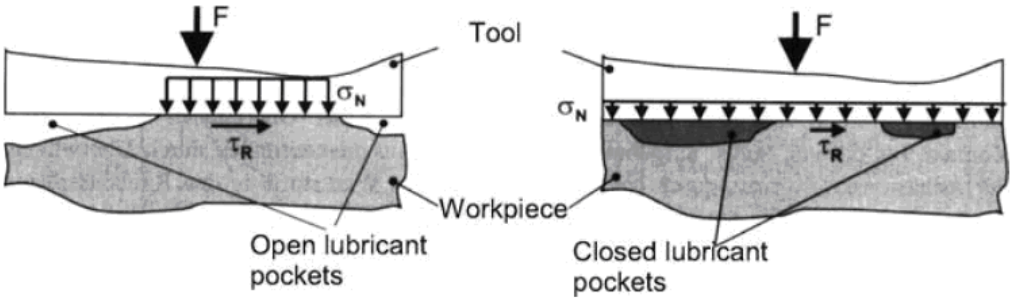

FIGURE 2.4: Description of open and close lubricant pockets [6]

of 0.48 mm using 1.2 mm diameter billets, respectively. The experiments were conducted using billets of different average grain sizes. They investigated also effect of surface roughness by using extrusion dies of different surface roughness. Their experimental results suggest that the extrusion force is independent from the surface texture. Furthermore force-displacement curves are fairly repeatable.

As far as modelling polycrystalline material behaviour at micro-scale is concerned, it is important to emphasize the fact that conventional plasticity models can not capture grain orientation and slip systems of the unit cell. To investigate the possibilities to use conventional material models, Meisner[14] proposed the concept and use of size dependent flow curves. A FE model of a ring compression test is constructed in which the specimen is subdivided into a surface region and an inner region. For the surface region, flow curves obtained from upsetting experiments of 1 mm diameter specimens whereas for the inner region the conventional flow curves are used.

Another approach proposed by Geissdörfer [15] was based on the combination of a grain level model with grain specific flow curves. The flow curve for a particular grain is determined by means of the Hall-Petch relation and micro upsetting tests were modelled and compared with experimental results. Their findings indicate that the approach can capture the scatter in characteristics outputs. However, the orientation of individual grains and the underlying crystal structure were all ignored.

Cao et al. [13], along with their experimental work, conducted modelling studies, where they used the meshless method (Reproducing Kernel Element Method), to circumvent the excessive mesh distortion and remeshing issues.

Since the orientation of individual grains become decisive when the average grain size is large as compared to the component size, the crystal plasticity theory proposed in Asaro et al. [16], is suitable framework to capture peculiarities observed in micro-extrusion experiments.

There is large body of references on crystal plasticity and its use in different fields. In the context of micro-forming processes, Sarma et al. [17] have proposed the use of models where grain level resolution is combined with crystal plasticity theory. For very thin sheet metals, Fulop et al. [10] investigated the mechanical response using crystal plasticity and geometric grain structure generated by Voronoi tessellations. This framework allows one to carry out computational experiments to investigate, for example the influence of the number of surface grains to the total number of grains. In the context of ultra thin sheets, it is important to understand the influence of the number of grains in the thickness direction.

CHAPTER 3

EXPERIMENTAL SETUP

In order to demonstrate the statistical size effect and investigate the peculiarities of micro-forming, an experimental set-up for micro-extrusion has been designed and micro-extrusion tests with copper billets of different average grain sizes, have been conducted. In this chapter, the components of the experimental set-up, the design process and the experimental results are presented.

Throughout the study, the experimental set-up has evolved starting from the first version shown in the figure 3.1.

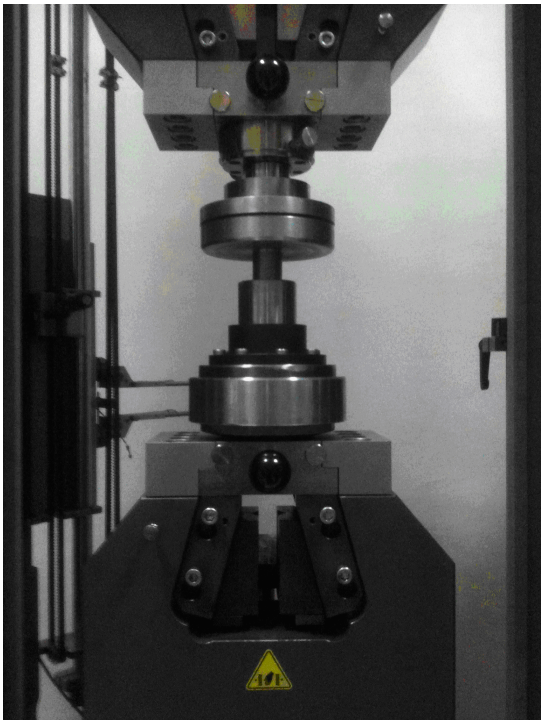

FIGURE 3.1: First presentation of experimental set-up.

Essentially the experimental set-up has four components namely, the micro-extrusion die, punch, the billet (work piece) and the press as shown in figure 3.1. Since the capacity of the Zwick compression /tension machine available at Metal Forming Center of Excellence (MFCE) is sufficient for micro-extrusion process, the set-up is designed and dimensioned considering a vertical press layout. The stationary flange is hosted by the lower plate of the Zwick compression/tension tester and the extrusion force is supplied by the upper flange which is pushed by the upper plate (cross-head) of the machine. In figure 3.2 the overall layout of the set-up is presented. In the following subsections, each component is elaborated.

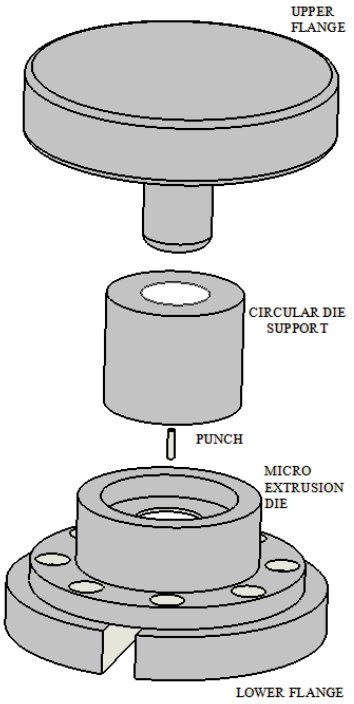

FIGURE 3.2: The overall layout of the micro-extrusion die.

3.1 Lower Flange

The geometry and picture of the lower flange is shown in figure 3.3. Lower flange is designed to hold the die and rear surface is tightly sitting on the lower circular plate of the tension/compression machine. The components is manufactured at Elfa Metal and made of 1040 class steel.

3.2 Circular Die Support

Since the set-up is designed in a vertical configuration, sufficient height has to be supplied to receive the extruded material at the end of the process. To this end, an annular circular die support, see figure 3.4, is used to elevate the die. Similar to the lower flange, the component is made of 1040 class steel.

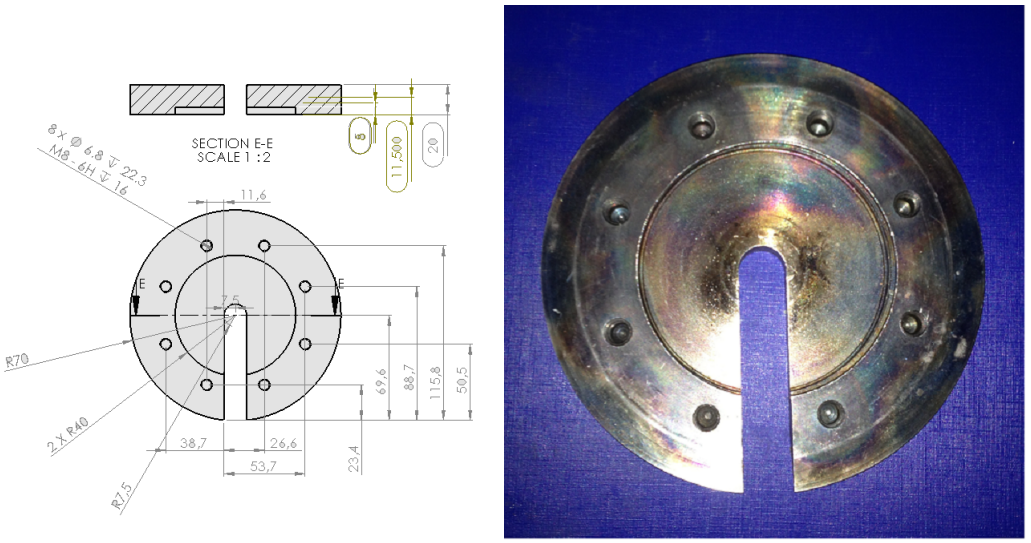

FIGURE 3.3: The geometry and picture of the lower flange

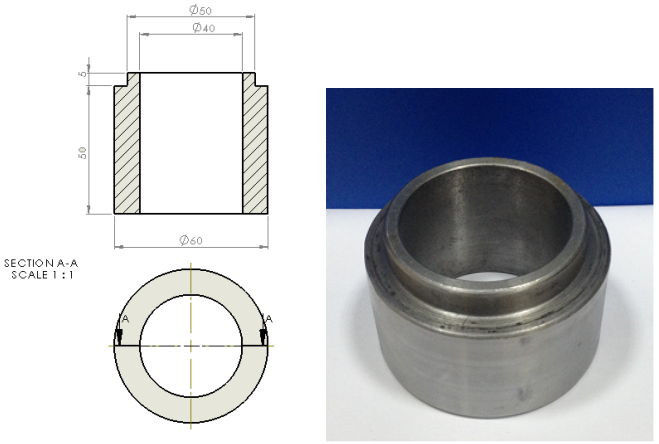

FIGURE 3.4: The geometry and picture of the circular die support

3.3 Micro-Extrusion Die

One of the most critical component of the set-up is the die. Throughout the study, two different dies are designed and manufactured. The first version, which is called as “the laterally segmented die” is designed such that two semi cylindrical parts are machined according to the extrusion cavity geometry and then combined, see figure 3.5. Due to the relative easiness in manufacturing the segmented die was preferred. However, it turned out that the press forces are large enough to deform the die parts in radial direction and due to large geometrical distortions the process can not be done with this segmented die.

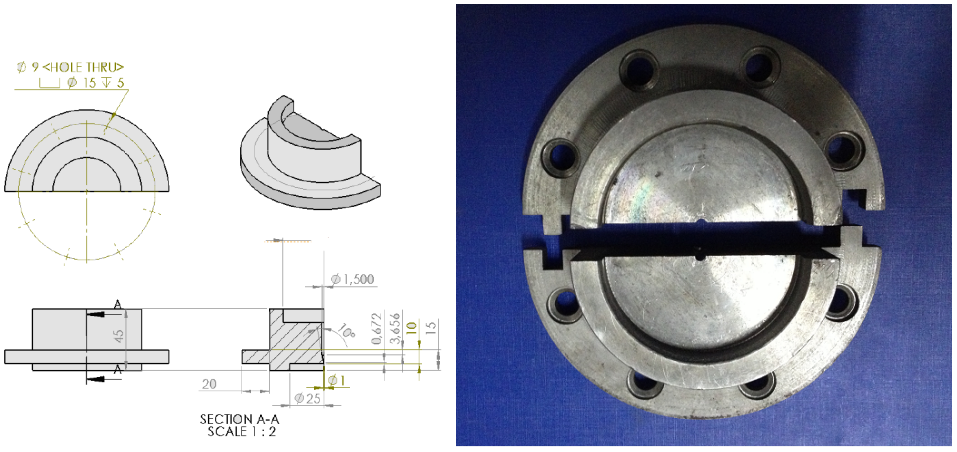

FIGURE 3.5: The geometry and picture of micro-extrusion die.

As an alternative, a vertically segmented die with the same geometry is manufactured as shown in figure 3.6.

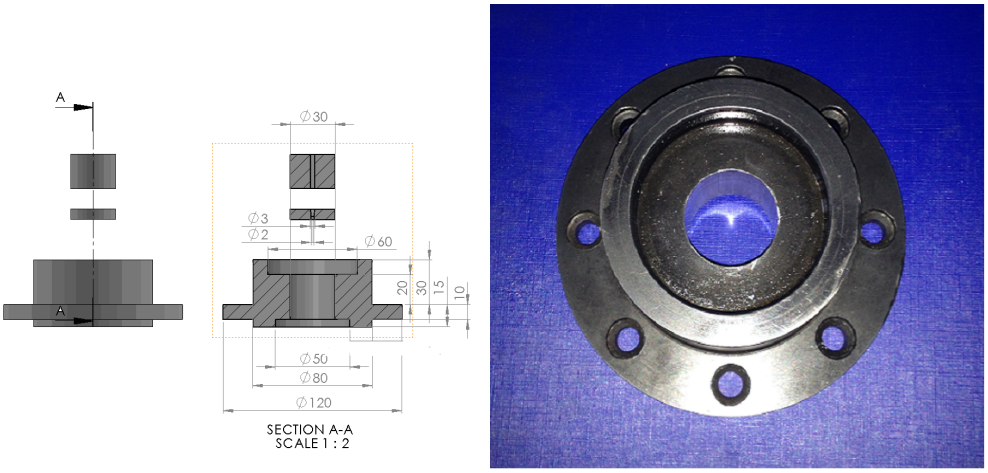

FIGURE 3.6: The alternative geometry and picture of micro-extrusion die.

Due to limitation of electrical discharge machining cutting operations, vertically segmented die is proposed which is composed of a cylindrical part with a centered cylindrical cavity and another part with a centered conical cavity as shown in figure 3.6. The die was machined from 2379 class steel which is then hardened by a heat process resulting in 55-60 Rock-well hardness.

3.4 The Punch

In terms of geometry, the punch used is relatively simple as shown in figure 3.7. Similar to the vertical segmented die heat treated 2379 class steel is used.

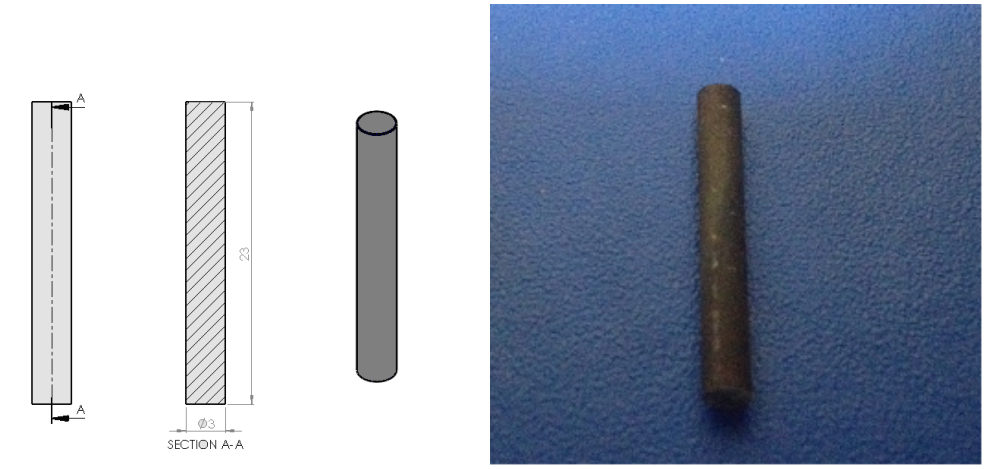

FIGURE 3.7: The geometry and picture of punch.

However, in the initial trials, the punch failed. The possible reason for failure is going to be considered in the next section. Due to failure, new punches were manufactured using Vanadis 39 class powder metallurgy steels.

3.5 The Upper Flange

The first version of upper flange is given figure 3.8. The circular top face of the component is machined such that the cross-head plate tightly fits to the flange. The punch is attached to the top flange and forced downwards by means of the force transmitted from the tension/compression machine.

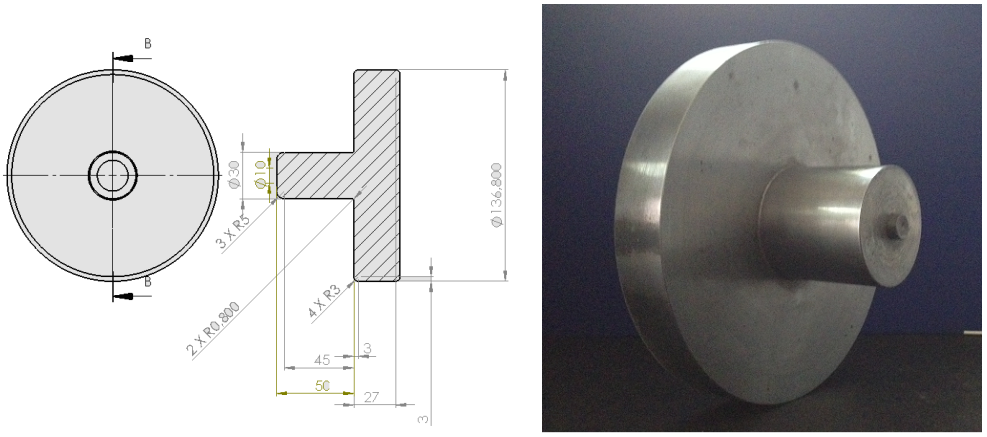

FIGURE 3.8: The geometry and picture of upper Flange

After the initial trials, it was realized that the set-up is very sensitive to lateral disturbances and the possible reason for the failure of the initial punches were bending induced due to the loss of centricity of the set-up. To remedy this problems, we add the part of support bottom flange to the set-up. The top flange has been modified such that the vertical motion of the component is guided by four vertical bars welded to the support bottom flange, see figures 3.9 and 3.10.

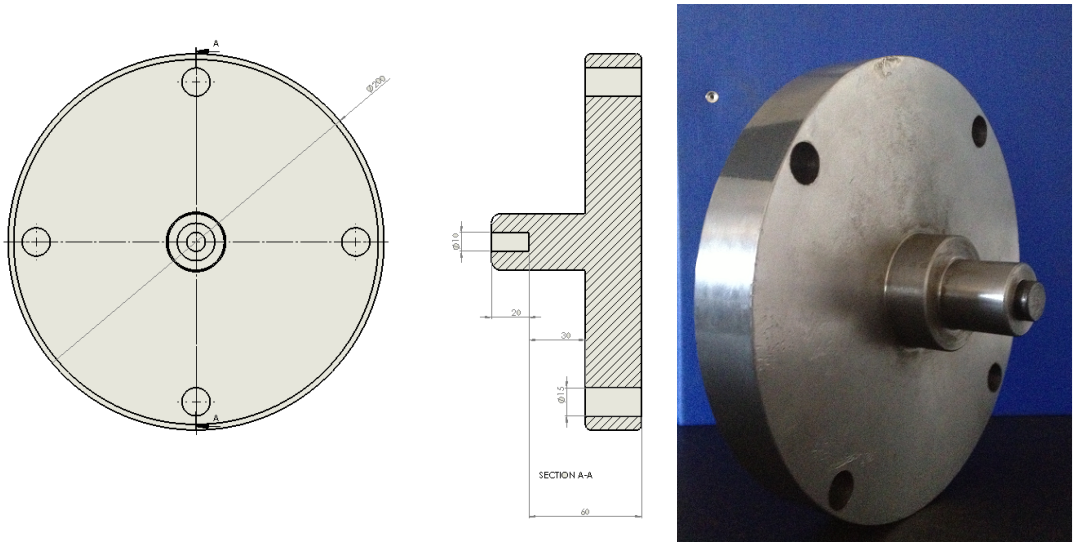

FIGURE 3.9: : The modified geometry and picture of upper Flange

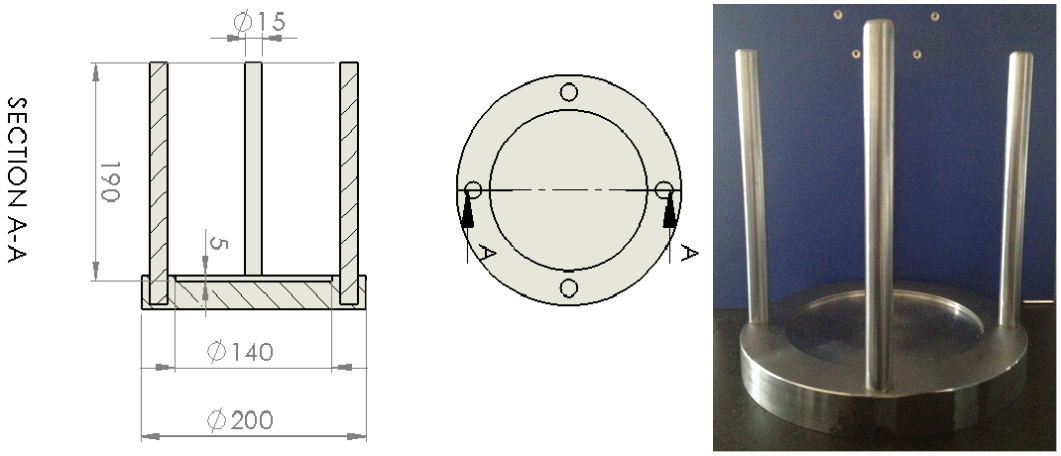

FIGURE 3.10: : The geometry and picture of support lower flange

With this modification, the final design which is shown in figure 3.11 and 3.12, is successfully used to conduct all the experiments.

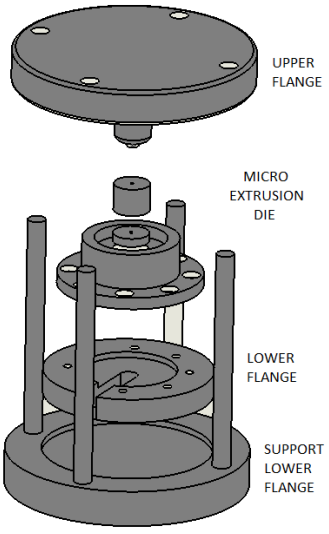

FIGURE 3.11: Final design of micro-extrusion die

FIGURE 3.12: Final picture of micro-extrusion die

3.6 Billet

Due to its high ductility and relatively low yield stress, copper billets are used in the experiments. The billets are cut from long copper wires of 3 mm diameter. The mechanical and thermal history of the wire is not known. As received micro-structure is shown in figure 3.13. The corresponding histogram of grain size distribution is given in figure 3.16.The average grain size is 13.9 μm.

Since the average grain size is not sufficient to capture the statistical size effect, the wires are further exposed to a heat treatment with a conventional laboratory oven and quenching in a water bath. Two different treatment procedures are followed. In the first case the billets are kept for 30 minutes in the oven at $700^{\circ}C$ and then immediately quenched. The resulting micro-structure is shown in figure 3.14 and these billets are labelled as billet A in the rest of the thesis.Similarly, the corresponding grain size distribution data is given in figure 3.17, from which the average grain size is calculated as 61.9 μm.

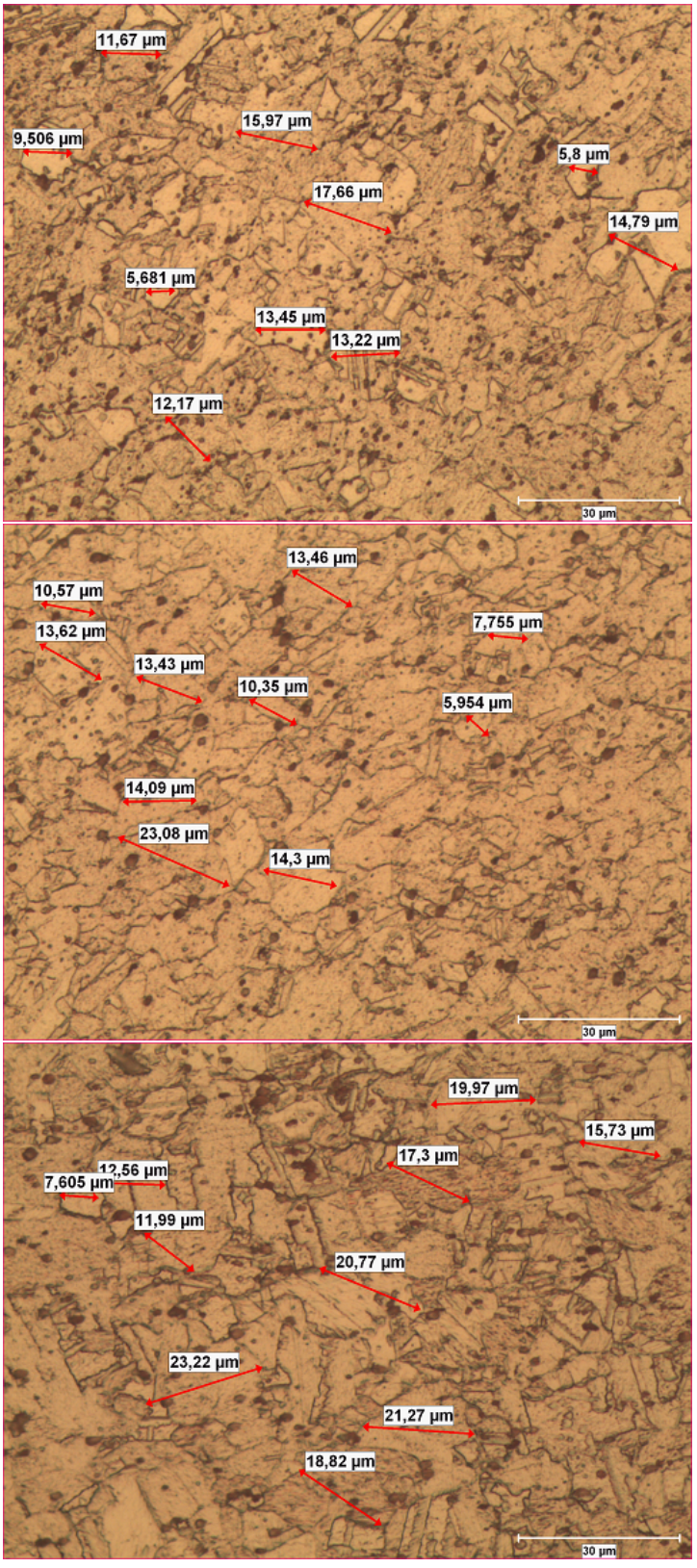

FIGURE 3.13: The micro-structure of the copper billet (As received)

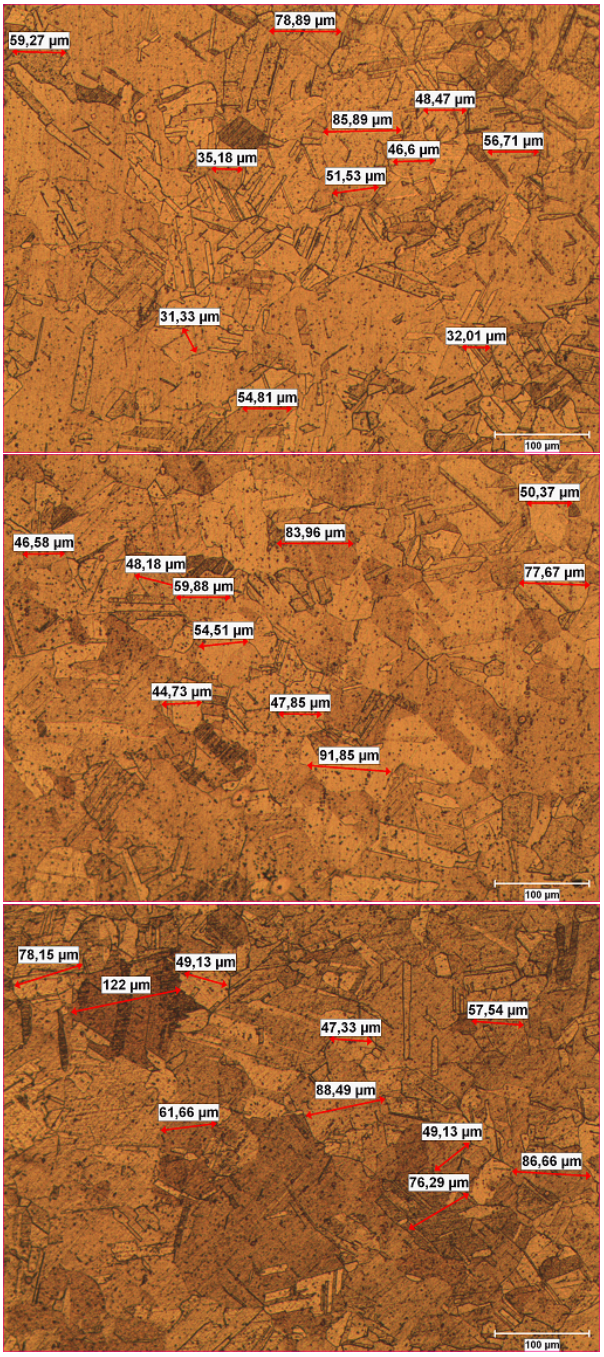

FIGURE 3.14: The micro-structure of the copper billet A

In the second treatment route, the billets are kept 120 minutes in the oven at 700°C and then immediately quenched. The resulting micro-structure is shown in figure 3.15 and these billets are labelled as billet B in the rest of the thesis. According to the histogram given in figure 3.6,from which the average grain size for billet B is about 79.4 μm.

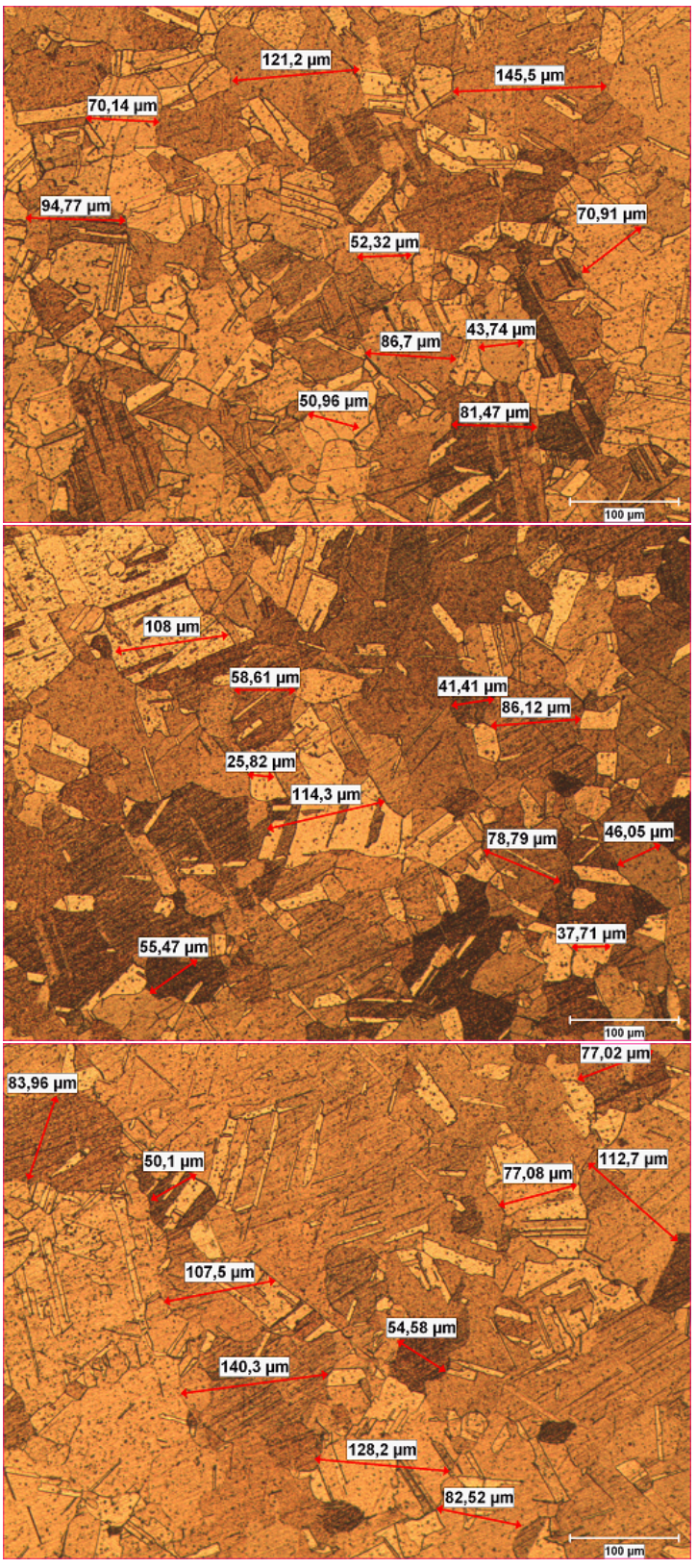

FIGURE 3.15: The micro-structure of the copper billet B

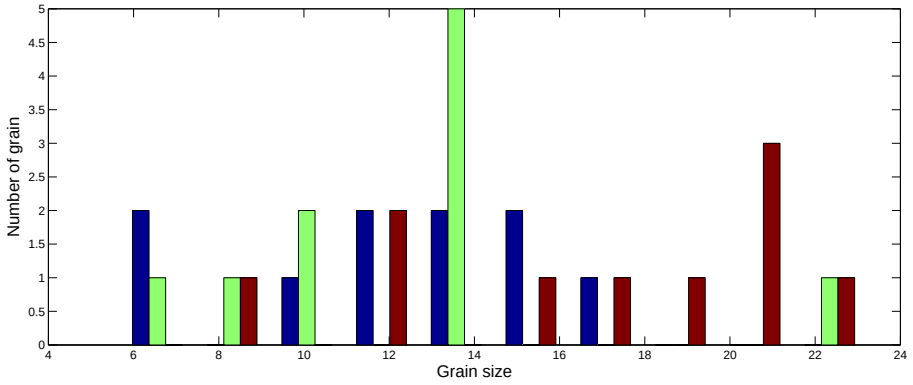

FIGURE 3.16: The histogram of the copper billet (As received)

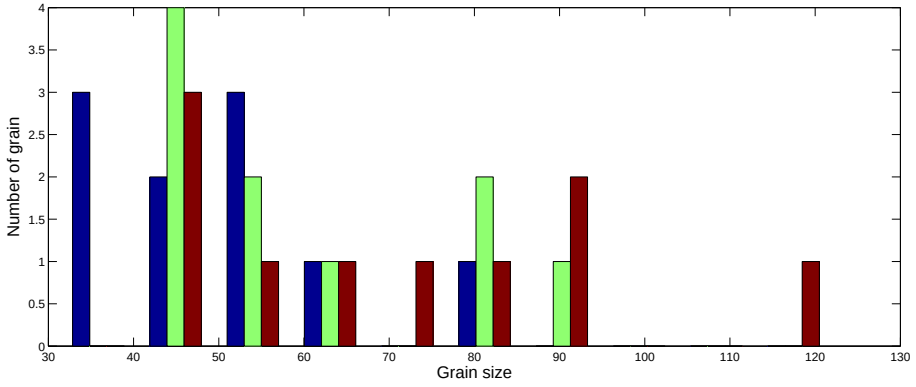

FIGURE 3.17: The histogram of the copper billet A

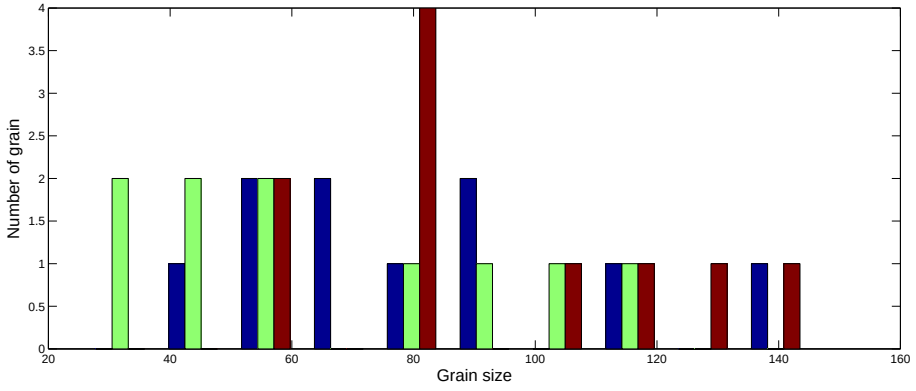

FIGURE 3.18: The histogram of the copper billet B

3.7 Experimental Procedure

The micro-extrusion experiments are conducted using the Zwick compression/tension test machine under displacement control. The cross-head speed was 10 mm/min. and typically a total displacement of 12 mm for the cross-head is prescribed. In the experiment, Würth HHS5000 is used as the lubricant and both the extrusion die and the billet are lubricated sufficiently. Experiments are conducted multiple times with both billet A's and billet B's. The force-displacement curves for the experiments with billet A are presented in figure 3.19.

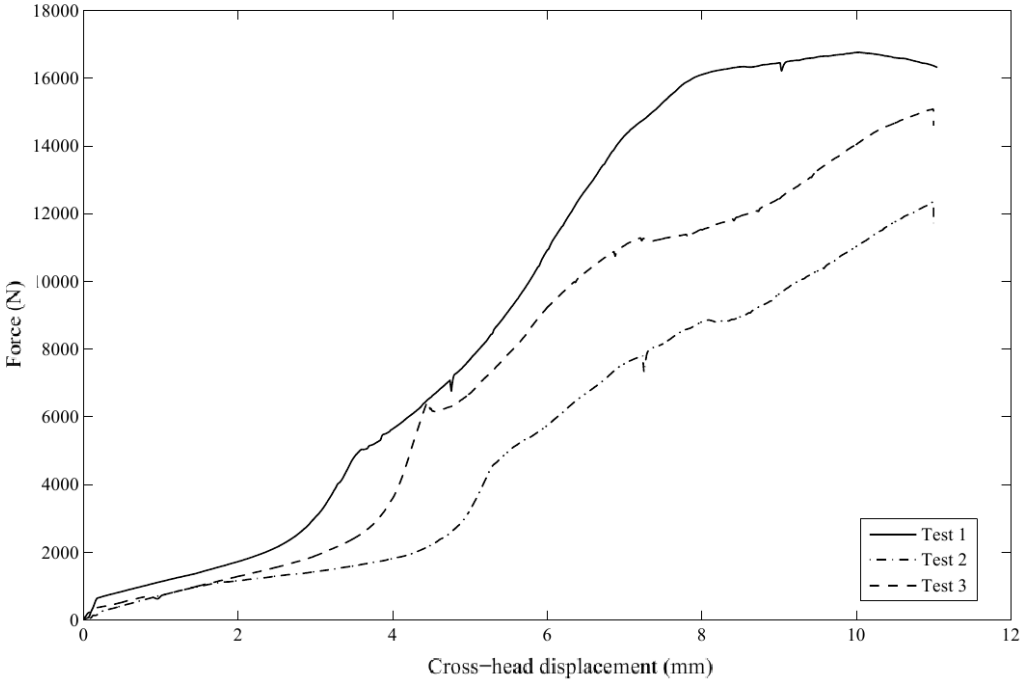

FIGURE 3.19: The force-displacement curves for the experiments with billet A

The extrudates of billet A's resulting from 3 different experiments are shown in figure 3.20.

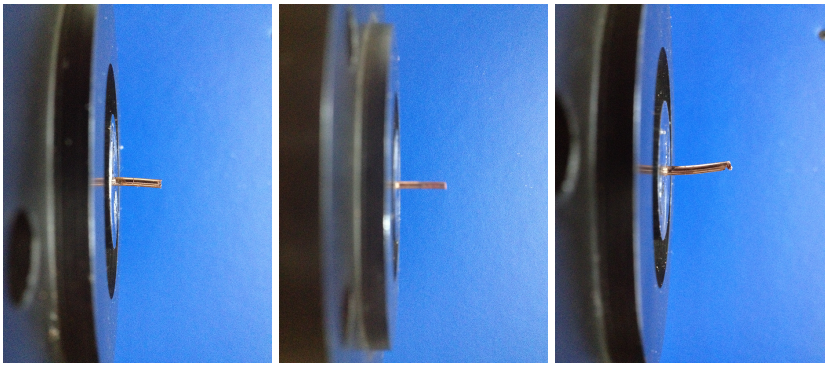

FIGURE 3.20: The extrudates of billet A's resulting from 3 different experiment

The Corresponding curves and pictures belonging to the billet B's are shown in figure 3.21 and 3.22 respectively.

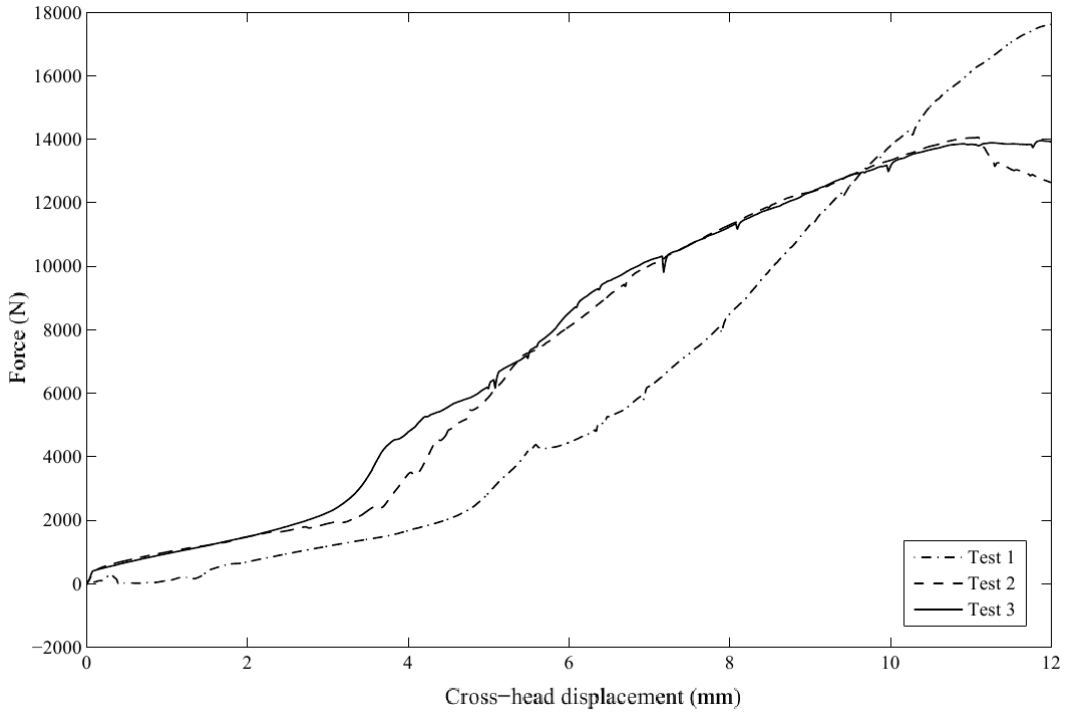

FIGURE 3.21: The force-displacement curves for the experiments with billet B

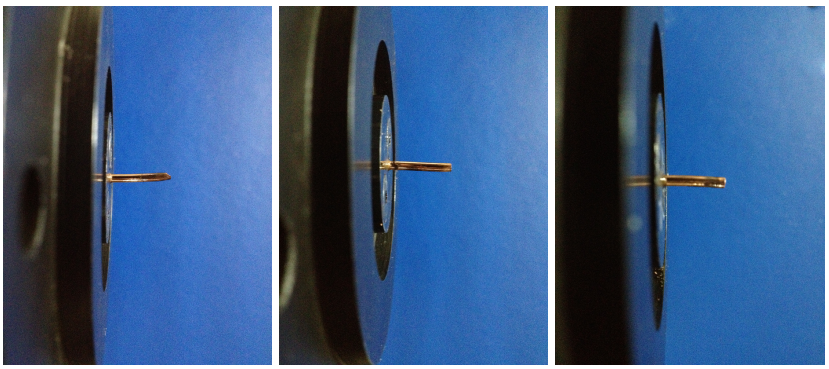

FIGURE 3.22: The extrudates of billet B's resulting from 3 different experiment

For both sets of the experimental result, there is significant scatter in force-displacement curves.There is a difference of approximately 4000 N in the peak load recorded in the experiments, see figure 3.19. As compared to the maximum peak load of 16000 N, this scatter is very large. A similar situation is observed for experimental curves obtained with billet B's. This time the difference is around 3500 N. However, two of the three curves are very close to each other, which makes it difficult to comment of these results. The bending of the extrudates can be clearly seen for a couple of tests.The magnitude of the bending effect is not quantified which has to be done with proper tools after getting sufficient number of experimental data. As the number of grains in the billet gets "countable", the properties of individual grains become decisive on the overall response. Since sample B's have larger average grain sizes, it was expected to see a more significant statistical size effect for the tests conducted with sample B's. An important point which has to be mentioned is the fact that the heat treatment and quenching operations are done at atmospheric pressure conditions. At high temperature, due to reactive nature of copper, it is expected that an oxide layer develops on the samples. The thickness of these layers might be uneven on the billet surface, which can be the other source of observed bending. Since lubricant is used during experiments, it is difficult to comment on the influence of oxide larger on the overall response. Therefore further tests with properly treated samples are necessary. Furthermore, by well defined and controlled heat treatment and quenching protocols, it would be possible to control the average grain size much better and desired average grain size can be

reached. By this way, it would be much easier to capture the statistical size effect in micro-extrusion process.

For each case, three micro-graphs considered are taken from different points on the sample.Actually the analysis can be improved by the increasing the number of sampling points. As a result, the experimental results presented are not sufficient to draw reliable conclusions. It is important to note that the developed experimental set-up is sufficient for further experimental investigations.

CHAPTER 4

MODELLING

Due to the large displacement and large strains developing in forming processes, a geometrically non-linear continuum mechanics description is used in this study. In what follows, basic continuum mechanics quantities are introduced since they are needed for subsequent developments. For a detailed and accessible treatment, one can consult to Bonet & Wood [20]. In figure 4.1, the reference and current configuration of a deformable body is shown. The placement of the reference material points is described by the motion function ϕ,

$$\underline{x}_t = \phi_t(\underline{X}) \tag{4.1}$$

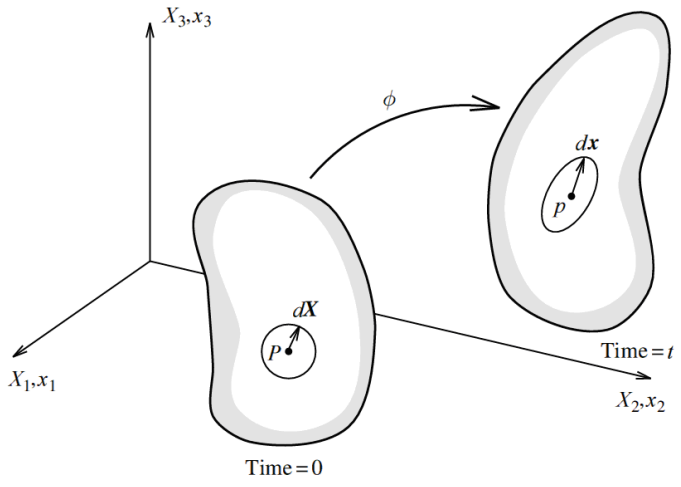

FIGURE 4.1: The reference and current configuration of a deformable body [20]

and the basic kinematical descriptive quantity is the deformation gradient which maps the reference material infinitesimal line segment to the current configuration by,

$$\underline{dx} = \underline{F}\,\underline{dX} \tag{4.2}$$

$\underline{F}$ is defined as,

$$\underline{F} = \nabla_{\underline{X}} \phi = \frac{\partial \phi}{\partial \underline{X}} \tag{4.3}$$

The velocity of a material point is the spatial vector which is tangent to the trajectory of the material point throughout the motion. In the current configuration the relative velocity of two different material points is defined by the velocity gradient tensor $\underline{l}$ as;

$$\underline{l} = \frac{\partial \underline{v}(\underline{x},t)}{\partial \underline{x}} = \nabla \underline{v} \tag{4.4}$$

Whose symmetric part defines the rate of deformation $\underline{d}$;

$$\underline{d} = \frac{1}{2}\left(\underline{l} + \underline{l}^T\right) \tag{4.5}$$

and the anti-symmetric part of $\underline{l}$ is called the spin tensor and defined as ;

$$\underline{w} = \frac{1}{2}\left(\underline{l} - \underline{l}^T\right) \tag{4.6}$$

There are different definition of strain measures depending on the configuration considered. The Lagrangian strain tensor which is defined on the reference configuration is given as;

$$\underline{E} = \frac{1}{2}\left(\underline{F}^T \underline{F} - \underline{I}\right) \tag{4.7}$$

Similar to strain measures, there are different stress definitions depending on the configuration considered. For example Cauchy stress tensor σ defined on the current configuration as,

$$\underline{t} = \lim_{\Delta a \to 0} \frac{\Delta \overrightarrow{p}}{\Delta a} = \underline{\sigma}\,\underline{n} \tag{4.8}$$

For the definition of $\Delta\overrightarrow{p}$ and $\underline{n}$, see figure 4.2.

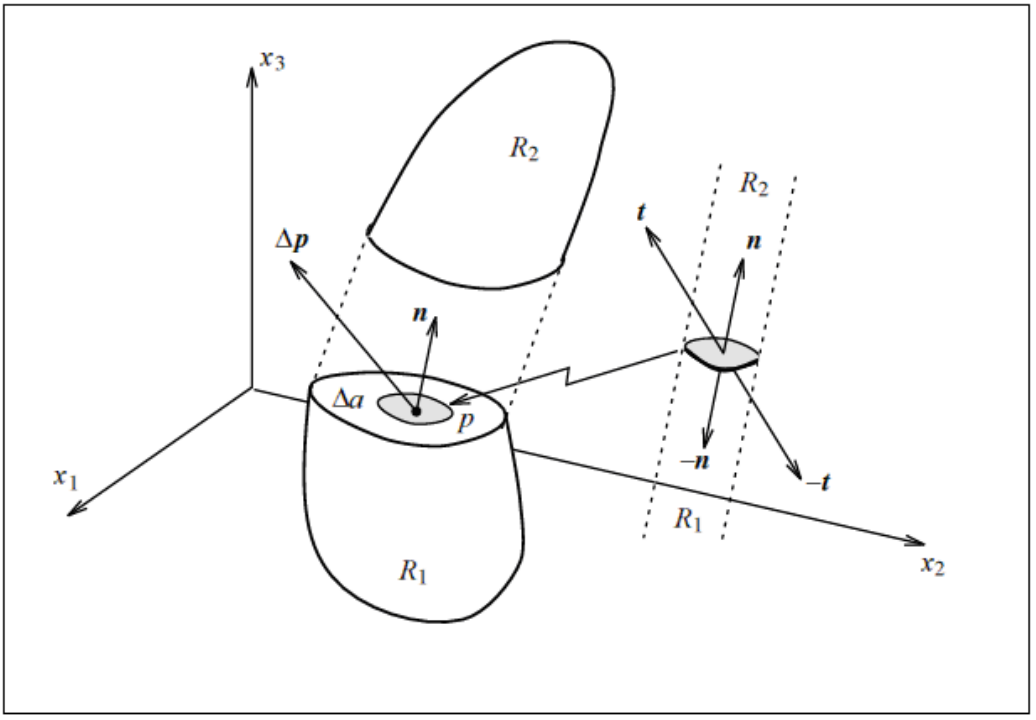

FIGURE 4.2: Traction vectors [20]

The 2^{nd} Piola Kirchhoff stress tensor is defined with respect to the reference configuration and related with Cauchy stress tensor as,

$$\underline{S} = \det \underline{F}\, \underline{F}^{-1} \underline{\sigma}\, \underline{F}^{-T} \tag{4.9}$$

The other commonly used stress tensor is the 1^{st} Piola Kirchhoff stress tensor $\underline{P}$ which is a mixed configuration quantity and related with Cauchy stress tensor as,

$$\underline{P} = \det \underline{F}\, \underline{\sigma}\, \underline{F}^{-T} \tag{4.10}$$

Considering a body which is under the action of body forces $\underline{b}$ and external traction applied on Γ_t the equilibrium equations in the current configuration is defined as;

$$\nabla \cdot \underline{\sigma} + \underline{b} = \underline{0} \tag{4.11}$$

where ∇ is the gradient operator with respect to current coordinates,

$$\nabla = \frac{\partial}{\partial \underline{x}} \tag{4.12}$$

Therefore the differential form of the problem is defined as,

$$\nabla \cdot \underline{\sigma} + \underline{b} = \underline{0} \quad \text{for every} \quad \underline{x} \in \mathrm{v} \tag{4.13}$$

$$\underline{\sigma} \cdot \underline{n} = \bar{\underline{t}} \quad \text{on} \quad \Gamma_t$$

$$\underline{u} = \bar{\underline{u}} \quad \text{on} \quad \Gamma_u$$

Since the closed form solution of the differential form is quite limited to very simple geometries and constitutive models, finite element method is used to obtain approximate solutions. However the FE solutions requires the variational or integral weak form of the differential equation. To this end ,the principle of virtual work is used to get the weak form of the problem which is given as ;

$$\int_v \underline{\sigma} : \delta \underline{d} \mathrm{dv} = \int_v \underline{f} \cdot \delta \underline{u} \mathrm{dv} + \int_{\partial v} \underline{t} \cdot \delta \underline{u} \mathrm{da} \tag{4.14}$$

for every $\delta \underline{u}$ where $\delta \underline{u} = 0 \quad on \quad \Gamma_u$.

For the intermediate steps one can consult to Bonet and Wood [20]

The integral equation 4.14 is completed with the use of a particular constitutive model which describes the stress response of the body under consideration. For inelastic constitutive models stresses are expressed typically in a rate form which describes the incremental stress tensor as a function of history variables and deformation. The particular model used in this work and the accompanying stress update algorithm is presented in the next section. Furthermore, due to geometric and material non-linearities,

equation 4.14 is solved by using an incremental-iterative solution procedure. This requires consistent linearisation of equation 4.14, which necessitates the derivation of the algorithmic tangent moduli of the stress update algorithm.

Since a grain level description is necessary for micro-forming operations, it is appropriate to use crystal plasticity to model the mechanical response of each grain. Therefore, in the next section, after some brief information on the lattice structure and slip systems, the continuum level crystal plasticity and the algorithmic details are presented to a certain extent.

4.1 Crystal Plasticity

4.1.1 Preliminaries

Solid materials can be classified with respect to the arrangement of atoms in material. A crystalline material is the one in which the atoms are placed in a periodic array over large atomic distance. Almost all metals, many ceramic materials forms a crystalline structure under normal solidification conditions.

The term of "lattice" can be used in the context of crystalline structure as three dimensional array of points which is coinciding with the position of atoms. The atoms can be thought as being solid spheres having well defined diameter.

In describing the lattice structure, it is often convenient to subdivide the structure into the small repeated entities called as unit cell. An example of FCC(face centered cubic) crystalline structure is given in figure 4.3

During plastic deformation, dislocations which are linear crystal line defects don't move with the same degree of ease on all crystal graphic planes of atoms and in all crystallographic directions. There is a preferred plane and specific direction along which dislocation motion occurs. This plane is called as slip plane and the direction of the movement is called as the slip direction. The combination of the slip plane and slip direction is called a slip system. For a particular crystalline structure the slip plane is

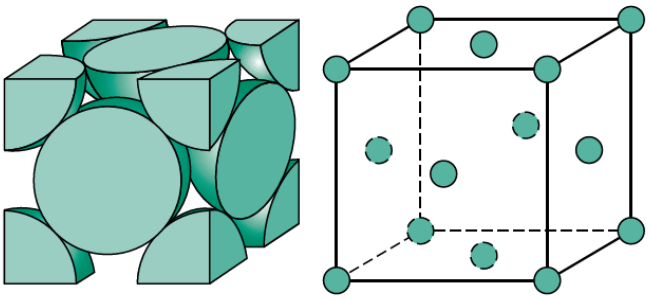

FIGURE 4.3: Representation of atoms for the face centered cubic crystal structure [21]

the plane that has the greatest atomic packing; in other words the one with the greatest planar density. For FCC crystalline structure, the set of slip planes and slip directions are shown in figure 4.4.

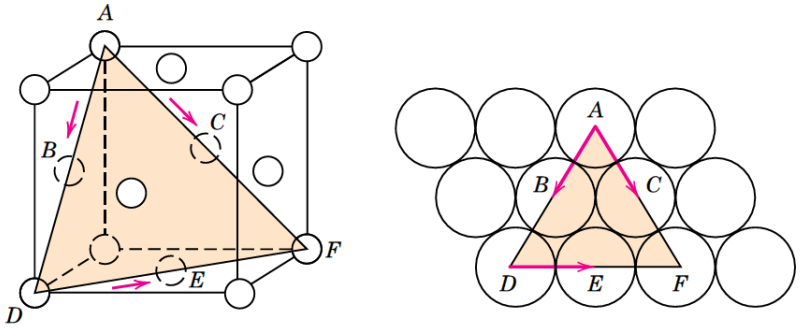

FIGURE 4.4: Representation of the slip plane and slip direction for FCC crystalline structure [21]

4.1.2 Kinematics in Crystal Plasticity

In continuum mechanics setting, the actual deformation with respect to the reference state is determined by the deformation gradient tensor $\underline{F}$. This tensor $\underline{F}$ is multiplicatively decomposed into an elastic part $\underline{F}_e$ and a plastic part $\underline{F}_p$ as ;

$$\underline{F} = \underline{F}_e \underline{F}_p \tag{4.15}$$

which is visualized in figure 4.5. The plastic deformation gradient represent microscopic sliding along the slip planes whereas the elastic deformation gradient indicates the crystal lattice distortion.

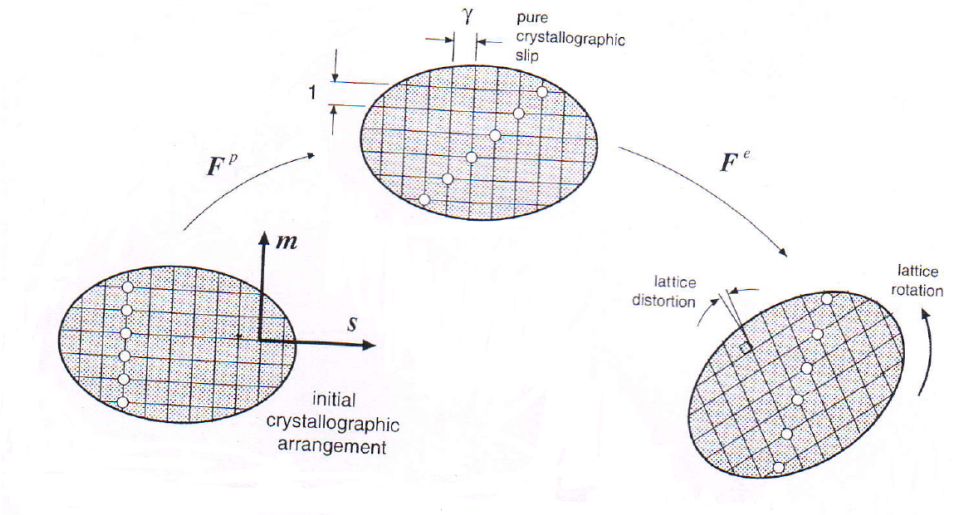

FIGURE 4.5: Decomposition of deformation gradient and the intermediate configuration [20]

The velocity gradient tensor $\underline{l} = \underline{\dot{F}}\,\underline{F}^{-1}$ is then decomposed as;

$$\underline{l}_e = \underline{\dot{F}}_e \underline{F}_e^{-1} \tag{4.16}$$

$$\underline{l}_p = \underline{\dot{F}}_p \underline{F}_p^{-1} \tag{4.17}$$

where $\underline{l}_e$ and $\underline{l}_p$ are called as elastic and plastic velocity gradient tensors, respectively. Using these tensor definitions and

$$\underline{\dot{F}} = \underline{\dot{F}}_e \underline{F}_p + \underline{F}_e \underline{\dot{F}}_p \tag{4.18}$$

$$\underline{F}^{-1} = \underline{F}_e^{-1} \underline{F}_p^{-1} \tag{4.19}$$

one can express the velocity gradient tensor $\underline{l}$ in the decomposed form as;

$$\underline{l} = \underline{l}_e + \underline{F}_e \underline{l}_p \underline{F}_e^{-1} \tag{4.20}$$

At this stage, it is convenient to introduce $\underline{s}_0$ and $\underline{n}_0$ which identify the unit vector in slip direction and slip normal for the unloaded state, respectively. Then $\underline{s}$ and $\underline{n}$ are the corresponding vectors for the current state which are defined as;

$$\underline{s} = \underline{F}_e \underline{s}_0 \tag{4.21}$$

$$\underline{n} = \underline{F}_e^{-T} \underline{n}_0 \tag{4.22}$$

Having defined slip system vectors, $\underline{l}_p$ is supposed to be the summed contribution by the individual slip systems as;

$$\underline{l}_p = \sum_{\alpha=1}^{n_s} \dot{\gamma}^\alpha \underline{s}_0^\alpha \underline{n}_0^\alpha \tag{4.23}$$

where $\dot{\gamma}^\alpha$ indicates the slip rate and α indicates the slip system. Therefore one can write

$$\underline{l} = \underline{l}_e + \sum_{\alpha=1}^{n_s} \dot{\gamma}^\alpha \underline{s}^\alpha \underline{n}^\alpha \tag{4.24}$$

for which equations 4.21 and 4.22 are used. Due to the second term in equation 4.24, the resulting $\underline{l}$ is antisymmetric and the plastic deformation is not spin free. Since the elastic strains are very small as compared to plastic strains in forming operations, Saint Venant Kirchhoff material model is used to describe the stresses which can be expressed as,

$$\underline{S} = \quad {}^4\underline{C} : \underline{E}_e \tag{4.25}$$

where $\underline{S}$ is the 2^{nd} Piola-Kirchoff stress tensor and $\underline{E}_e$ is the Elastic Green-Lagrange strain tensor defined with respect to the intermediate configuration. The explicit form of $\underline{E}_e$ is given as;

$$\underline{E}_e = \quad \frac{1}{2}(\underline{C}_e - \underline{I}) \quad \text{and} \quad \underline{C}_e = \quad \underline{F}_e^T \cdot \underline{F}_e \tag{4.26}$$

The fourth order tensor ${}^4\underline{C}$ is the isotropic elastic moduli which can be expressed as

$${}^4\underline{C} = K\underline{II} + 2G\left({}^4\underline{I} - \frac{1}{3}\underline{II}\right) \tag{4.27}$$

with K the bulk modulus and G the shear modulus. ${}^4\underline{I}$ is the symmetric 4^{th} order identity tensor. At this stage it is appropriate to remind the relations between Cauchy and Kirchhoff tensors which are given as;

$$\underline{\sigma} = \sum_{i,j=1}^{3} \sigma_{ij} e_i \otimes e_j \quad \text{and} \quad \underline{\tau} = J_e \cdot \underline{\sigma} \tag{4.28}$$

The driving force for the slip phenomena on individual slip system is the Schmidt stress which can be expressed as;

$$\underline{\tau}^\alpha = \underline{\tau} : (\underline{s}^\alpha \underline{n}^\alpha) = \underline{s}^\alpha \cdot \underline{\tau} \cdot \underline{n}^\alpha \tag{4.29}$$

Using equation 4.28; alternatively τ^α can be written as

$$\begin{aligned} &\underline{\tau}^\alpha = \underline{s}^\alpha \cdot \underline{\tau} \cdot \underline{n}^\alpha = \underline{s}^\alpha \cdot \underline{F}_e \cdot \underline{S} \cdot \underline{F}_e^T \cdot \underline{n}^\alpha = \\ &\underline{s}_0^\alpha \cdot \underline{C}_e \cdot \underline{S} \cdot \underline{n}_0^\alpha = \frac{1}{2}\underline{s}_0^\alpha \cdot \underline{C}_e \cdot [{}^4\underline{C} : (\underline{C}_e - \underline{I})] \cdot \underline{n}_0^\alpha \end{aligned} \tag{4.30}$$

4.1.3 Slip Evolution

As far as slip evolution is concerned, there are essentially two alternatives. In the first case, the slip evolution on individual slip planes is governed by a non-smooth

“yield function " similar to the case of multi-surface plasticity. However, this approach requires the determination of an active set of slip systems for which the existing approaches suffer from the uniqueness issue. Furthermore a well established robust algorithmic framework for active set determination does not exist. In the second case, the slip evolution is described by a constitutive law, for which in this work the following form

$$\dot{\gamma}^{\alpha} = \dot{\gamma}_0^{\alpha} \quad \frac{\tau^{\alpha}}{\tau_c^{\alpha}} \left(\frac{|\tau^{\alpha}|}{\tau_c^{\alpha}} \right)^{m-1} \tag{4.31}$$

is used. In this evolution law, τ_c^{α} is the resistance against slip on system α and m is the model parameter. In this work, a relatively simple and phenomenological slip resistance law

$$\tau_c^{\alpha} = \sum_{\beta=1}^{n_s} h^{\alpha\beta} |\gamma^{\beta}| \quad for \quad \alpha = 1, 2 \cdots, n^s \tag{4.32}$$

is used. In this equation $h^{\alpha\beta}$ can be considered as the hardening parameter for which, the following form is adopted

$$h^{\alpha\beta} = h^{\beta} \left(q + (1-q)\, \delta^{\alpha\beta} \right) \tag{4.33}$$

where h^{β} is the actual self hardening modulus and q is the latent-hardening.

4.1.4 Stress Update Algorithm

Assuming that ,within a typical time increment

$$t_n \leq t \leq t_{n+1} = t_n + \Delta t$$

the slip rates are constant; one can write

$$\dot{\underline{F}}_p \cdot \underline{F}_p^{-1} = \underline{l}_p = \frac{1}{\Delta t} \sum_{\alpha=1}^{n_s} \Delta\gamma^\alpha \underline{s}_0^\alpha \underline{n}_0^\alpha \tag{4.34}$$

The integration of equation 4.34, in combination with the approximation of the exponent of a tensor (see De Souza Neto et al.[18]) leads to

$$\underline{F}_p^{n+1} \cong \left(\underline{I} + \sum_{\alpha=1}^{n_s} \Delta\gamma^\alpha \underline{s}_0^\alpha \underline{n}_0^\alpha \right) \underline{F}_p^n \tag{4.35}$$

which gives the updated $\underline{F}^{n+1}$, provided that $\Delta\gamma^\alpha$' s are available.

Having determined the plastic part of the deformation gradient $\underline{F}^{n+1}$, the elastic part $\underline{F}_e^{n+1}$ follows from;

$$\underline{F}_e^{n+1} = \underline{F}^{n+1} \cdot \left(\underline{F}_p^{(n+1)} \right)^{-1} \tag{4.36}$$

Once $\underline{F}_e^{n+1}$ is obtained by using equation 4.28, one can determine the Cauchy stresses and the Schmidt stresses respectively. Using the Backward Euler integration scheme for $\dot{\tau}_c^\alpha$; $(\tau_c^\alpha)_{n+1}$ can be calculated as

$$(\tau_c^\alpha)_{n+1} = (\tau_c^\alpha)_n + \sum_{\beta=1}^{n_s} h^{\alpha\beta} |\Delta\gamma^\beta| \quad for \quad \alpha = 1, 2, \cdots, n_s \tag{4.37}$$

Enforcing the fulfilment of slip evolution laws at the end of the time increment, leads to the following form for equation 4.31,

$$\dot{\gamma}^\alpha - \dot{\gamma}_0^\alpha \quad \frac{\tau_{n+1}^\alpha}{(\tau_c^\alpha)_{n+1}} \left(\frac{|\tau_n^\alpha|}{(\tau_c^\alpha)_{n+1}} \right)^{m-1} = 0 \tag{4.38}$$

and have to be satisfied by each combination of τ^α and $(\tau_c^\alpha)_{n+1}$.

Equation 4.38 represents system of the non-linear equation which can be solved by the Newton-Raphson solution algorithm. Once the converged solution is obtained, $\underline{F}_p^{n+1}$

- $\underline{F}_{n+1}$, History variables
- Assume that $\gamma^{\alpha}_{n+1} = \gamma^{\alpha}_{n}$ elastic prediction
- Solve equation 4.38 by Newton-Rapson
- Obtain γ^{α}_{n+1}
- Obtain $\underline{F}^{n+1}_{p}$, $\underline{F}^{n+1}_{e}$
- Obtain $\underline{\sigma}_{n+1}$
- Obtain algorithmic tangent moduli ${}^{4}\underline{C}$
- Upon convergence, update history variables

FIGURE 4.6: Newton Raphson solution algorithm

and in turn $\underline{F}^{n+1}_{e}$ can be evaluated. The general outline of the solution procedure at a material point is given in figure4.6.

4.2 Orientation Description

In the following numerical investigation, single grain and multiple grain assemblies with arbitrary crystal orientations are considered. Therefore it is essential to characterize and describe the orientation of individual grain properly. To define an orientation, there must two frames; a reference frame attached to the specimen C_s and a frame attached to the crystal (grain) C_c, see figure 4.7. Typically, the reference frame is aligned with a characteristic axes of the specimen such as the rolling direction, transverse direction and normal direction for a rolled product. The crystal frame is aligned with important axes of the crystal, for cubic crystals, The [100], [010] and [001] axes. Both reference frames are orthogonal.

The orientation of the crystal is defined as the rotational position of the crystal frame with respect to the reference frame. There are many equivalent orientation descriptors. In this work, Euler angles and the associated rotation matrices are used for this purpose.

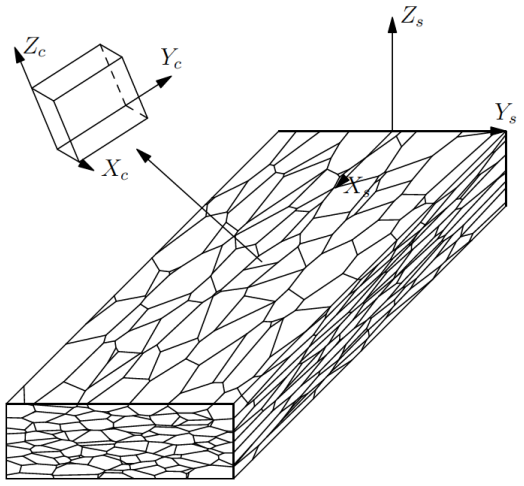

FIGURE 4.7: Reference Frame C_s and C_c [22]

4.2.1 Euler Angles

The Euler angles, expressed in Bunge Convention (φ_1,ϕ,φ_2), define an orientation through three successive rotations about different axes. In figure 4.8, the intermediate stages of the rotation of the specimen reference frame into the reference the crystal is shown successively.

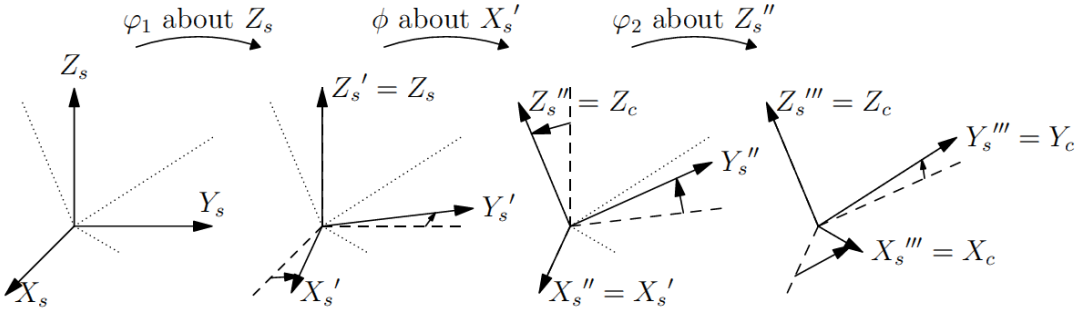

FIGURE 4.8: The rotation of the specimen reference frame into the reference of the crystal frame through Euler angles. Solid line: current frame, dash line: previous frame, dot line: final frame [22].

Typically the angles are defined such that $\varphi_1 \in [0,360]$, $\phi \in [0,180]$, $\Phi \in [0,360]$. Furthermore, it must be noted that, if $\phi = 0$, then rotations 1 and 3 are about the same axes and only the sum of φ_1 and φ_2 matters.

Provided that the Euler angles for each crystal(grain) are defined, the transformation between the crystal and reference frames are achieved by means of the rotation matrix $\underline{g}$ which is defined as,

$$\begin{bmatrix} x_c \\ y_c \\ z_c \end{bmatrix} = \begin{bmatrix} g_{11} & g_{12} & g_{13} \\ g_{21} & g_{22} & g_{23} \\ g_{31} & g_{32} & g_{33} \end{bmatrix} \begin{bmatrix} x_s \\ y_s \\ z_s \end{bmatrix} \tag{4.39}$$

Its rows contain the coordinates of the crystal frame vectors in the reference frame, and similarly, its columns contain the coordinates of the reference frame vectors in the crystal frame. Since, the reference and crystal frames are orthogonal, $\underline{g}$ is orthonormal and only three parameters are required to define it.

Conversion of Euler angles into rotation matrix are given as

$$g_{11} = \cos\varphi_1 \cos\varphi_2 - \sin\varphi_1 \sin\varphi_2 \cos\phi \tag{4.40}$$

$$g_{12} = \sin\varphi_1 \cos\varphi_2 + \cos\varphi_2 \sin\varphi_2 \cos\phi \tag{4.41}$$

$$g_{13} = \sin\varphi_2 \sin\phi \tag{4.42}$$

$$g_{21} = -\cos\varphi_1 \sin\varphi_2 - \sin\varphi_1 \cos\varphi_2 \cos\phi \tag{4.43}$$

$$g_{22} = -\sin\varphi_1 \sin\varphi_2 + \cos\varphi_1 \cos\varphi_2 \cos\phi \tag{4.44}$$

$$g_{23} = \cos\varphi\phi \tag{4.45}$$

$$g_{31} = \sin\varphi_1 \sin\phi \tag{4.46}$$

$$g_{32} = -\cos\varphi_1 \sin\phi \tag{4.47}$$

$$g_{33} = \cos\phi \tag{4.48}$$

In this work, grain orientations are described in terms of Euler angles and the finite element implementation of the model is based on the rotation matrix given by equation 4.39.

4.3 FE Modeling

The aforementioned crystal plasticity model is implemented within the commercial FE program Abaqus as a user defined material model through UMAT subroutine. The implicit incremental-iterative solution framework requires a consistent linearisation of the discrete equilibrium equations,

$$\underline{r} = \underline{f}_i - \underline{f}_e \tag{4.49}$$

$$\underline{r}|_k + \frac{\partial \underline{r}}{\partial \underline{u}}|_k \cdot \partial \underline{u} = \underline{0} \tag{4.50}$$

$$\partial \underline{u} = \underline{K}|_k^{-1} \cdot \underline{r}|_k \tag{4.51}$$

by which the iterative corrections $\partial \underline{u}$ column is calculated and the unknowns of the system are updated. The linearisation procedure requires the computation of the algorithmic tangent moduli. This tedious task is not detailed here.The interested reader can consult to [18].

In the modelling phase, quadratic brick elements with reduced integration (Abaqus element type C3D20R) is used due to their lower computational cost and good performance in incompressible deformation modes.

The implicit solution algorithm is summarized in figure 4.9. Therefore, stress update algorithm and the accompanying algorithmic tangent moduli are the two necessary outputs that have to be passed to the main program from the user subroutine UMAT. The updated stresses contributes to the internal force column $\left(\underline{f}_i^{(e)}\right)$ through the $\underline{B}^T \underline{\sigma}$ term and the algorithmic tangent moduli contributes to the element tangent stiffness $\left(\underline{K}_t^{(e)}\right)$ through $\underline{B}^T {}^4\underline{C}\, \underline{B}$ term. For convergence check, the default tolerances of Abaqus are used.

- Start of increment
  - Loop over elements
    $\underline{f}_i^{(e)} \leftarrow \underline{0}, \underline{K}_t^{(e)} \leftarrow \underline{0}$
    - Loop over integration points
    - Calculate $\underline{F}_{n+1}$, and get history variables
    - Assume that $\gamma_{n+1}^{\alpha} = \gamma_n^{\alpha}$ elastic prediction
    - Solve equation 4.38 by Newton-Rapson
    - Obtain γ_{n+1}^{α}
    - Obtain $\underline{F}_p^{n+1}$, $\underline{F}_e^{n+1}$
    - Obtain $\underline{\sigma}_{n+1}$
    - Obtain algorithmic tangent moduli ${}^4\underline{C}$
    - Add contribution to internal force column $\underline{f}_i^{(e)}$ and element stiffness matrix $\underline{K}_i^{(e)}$;
      $\underline{f}_i^{(e)} = \underline{f}_i^{(e)} + \underline{f}_i^{(ip)}$
      $\underline{K}_i^{(e)} = \underline{K}_i^{(e)} + \underline{K}_i^{(ip)}$
    - End of loop over integration points
  - Assemble $\underline{f}_i^{(e)}$ and $\underline{K}_i^{(e)}$ to the global system
  - End of loop over elements.
- Check for equilibrium
  - if satisfied go to end of increment
  - else
    - Solve the system and get the corrected nodal displacements
    - Go to the start of increment
- End of increment
- Update history variables
- Start of new increment

FIGURE 4.9: FE solution algorithm

In the analyses presented in the next chapter, the contact between the work-piece and the rigid die is assumed to be of Coulomb type. The Coulomb friction model has a non-smooth structure stating that

$$\text{if } \| \underline{t}_t \| < \mu \cdot t_N; \quad sticking$$
$$\text{if } \| \underline{t}_t \| = \mu \cdot t_N; \quad sliding$$

where $\underline{t}_t$ is the tangential component of the contact traction and t_N is the normal component of the contact traction. The contact tractions result in contact forces which has to be taken into account in the equilibrium equations. The treatment of contact contribution is out of the scope of this thesis work and interested read can consult to [19].

4.4 Numerical Investigation on Micro-scale Friction

An important aspect which has not been carefully and properly investigated in the literature so far, is the influence of grain orientation on the frictional response during micro-extrusion process. In order to have a better understanding, a series of numerical experiments are realized and presented in this section. To this end, the crystal plasticity framework presented in the previous section has been coded as a user defined material model and integrated into the commercial FE software Abaqus as a UMAT subroutine.

In the following sections, the implementation has beeen checked by single grain deformation tests and afterwards numerical experiments with single and multiple grain assemblies are presented.

4.4.1 Deformation of a Single Grain

In order to demonstrate the capabilities of the presented material model, a series of uni-axial tension tests on single grains are conducted. At first, to investigate and at the same time to check the implementation, certain slip systems are de-activated by assigning very large slip resistances (τ_c^α) to these systems. In figure 4.11, 4 different cases are shown where in each case, slip systems 1-2-3; 4-5-6; 7-8-9 and 10-11-12 are activated, respectively; for slip system definition see figure 4.10.

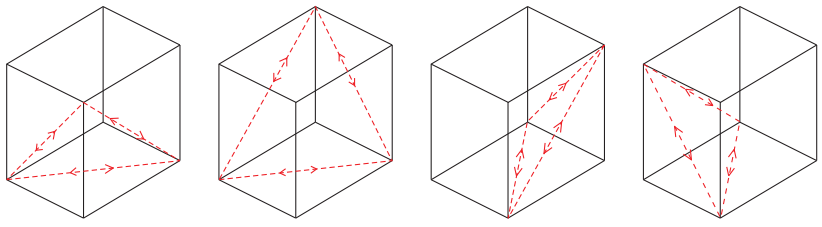

(a) Slip systems 1-2-3 (b) Slip systems 4-5-6 (c) Slip systems 7-8-9 (d) Slip systems 10-11-12

FIGURE 4.10: Slip systems

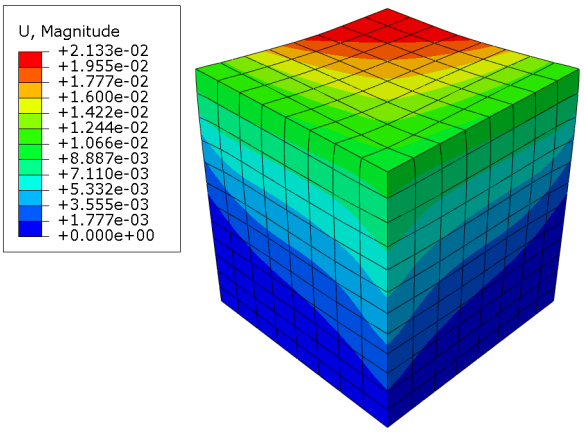

(a) Slip systems 1-2-3 are active

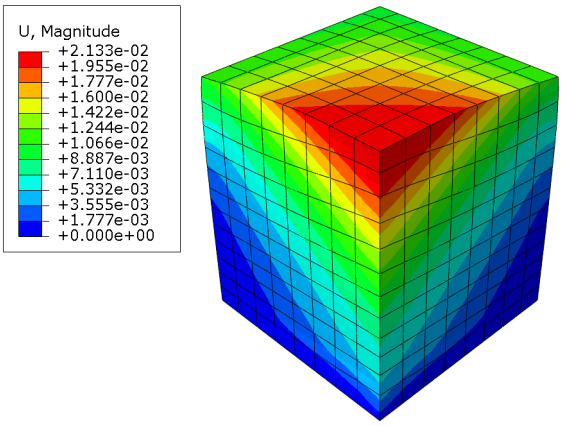

(b) Slip systems 4-5-6 are active

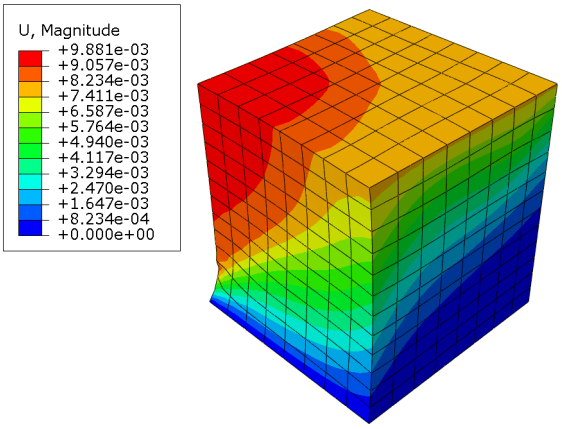

(c) Slip systems 7-8-9 are active

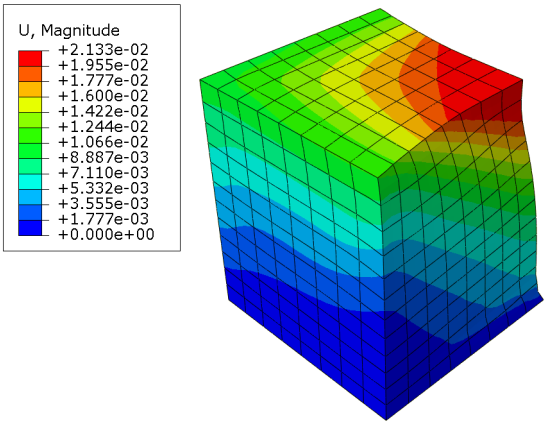

(d) Slip systems 10-11-12 are active

FIGURE 4.11: Deformed configurations under uni-axial tension

The activated slip systems are clearly reflected in the deformed configurations of the grains as shown in figure 4.11.

Furthermore, the implementation of the orientation description in terms of rotation matrices, is checked by the case where Euler angles are chosen as $\varphi_1 = 0$, $\phi = 45$, $\varphi_2 = 0$. This selection corresponds to a rotation of 45^o around the Y axis in counter clockwise direction. In figure 4.12 the deformed configuration of the rotated grain is presented on the right hand side which is in full agreement with the expected result.

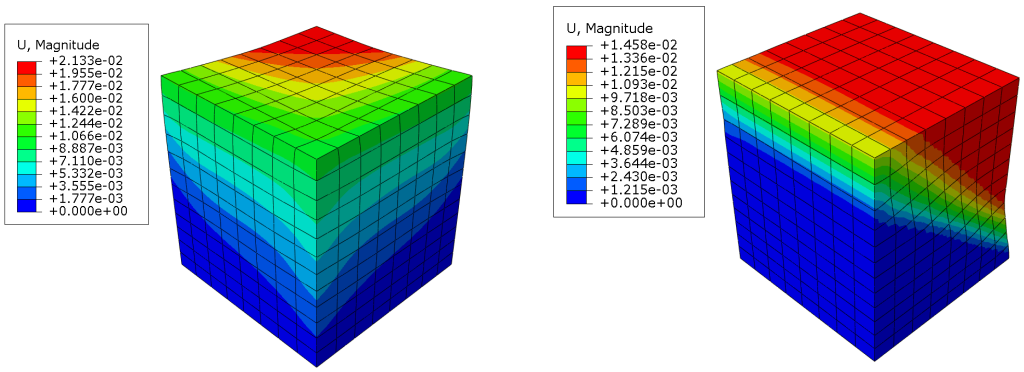

FIGURE 4.12: Deformed configurations; on the left $\varphi_1 = 0$, $\phi = 0$, $\varphi_2 = 0$; on the right $\varphi_1 = 0$, $\phi = 45$, $\varphi_2 = 0$

4.4.2 Case 1: Upsetting of a Single-Grain

To investigate the influence of grain orientation when there exists a frictional interaction between the work-piece and the tool, first a series of analysis on single grain with different orientation have been conducted. A cubic grain of $0.1mm \times 0.1mm \times 0.1mm$ has been discretized by 768 reduced integrated quadratic elements. The rigid top plate has been pushed downward by $0.01mm$. The contact between the grain and the rigid plate is assumed to be of Coulomb type with a coefficient of friction, $\mu = 0.1$. The boundary conditions imposed on the cube is shown in figure 4.13.

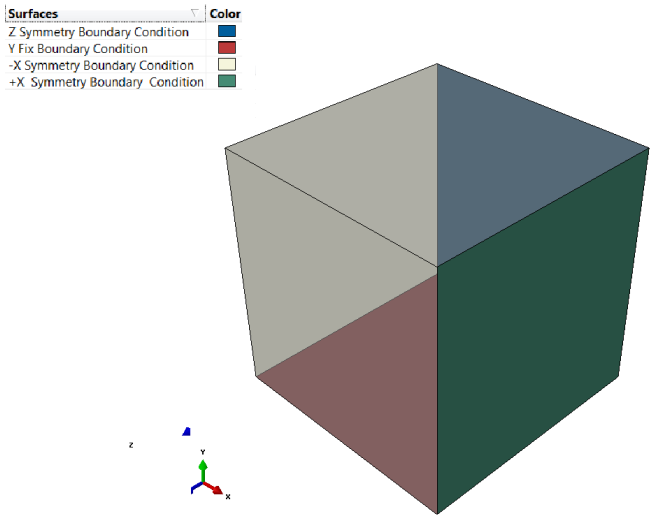

FIGURE 4.13: The boundary conditions imposed on the cube

Five analysis with different orientations have been realized. The material properties used and the Euler Angles of the orientations are given in table 4.1 and table 4.2, respectively.

Material properties	
$E\,(MPa)$	120000
v	0.3
$\dot{\gamma}_o$	0.001
m	4
$h\,(MPa)$	40
g	1.4

TABLE 4.1: Table of Material Properties

Grain ID	Euler Angles(^{o})		
	φ_1	ϕ	φ_2
Grain 1	229	62	116
Grain 2	344	140	282
Grain 3	86	121	169
Grain 4	243	1	12
Grain 5	104	108	63

TABLE 4.2: Euler Angles used in each analysis

In figures 4.14, 4.15, 4.16 the deformed state of the cubes for three different orientations are shown. Clearly, the inherent anisotropy reveals itself in a non-homogeneous deformation which can be seen both at top views and isometric views.

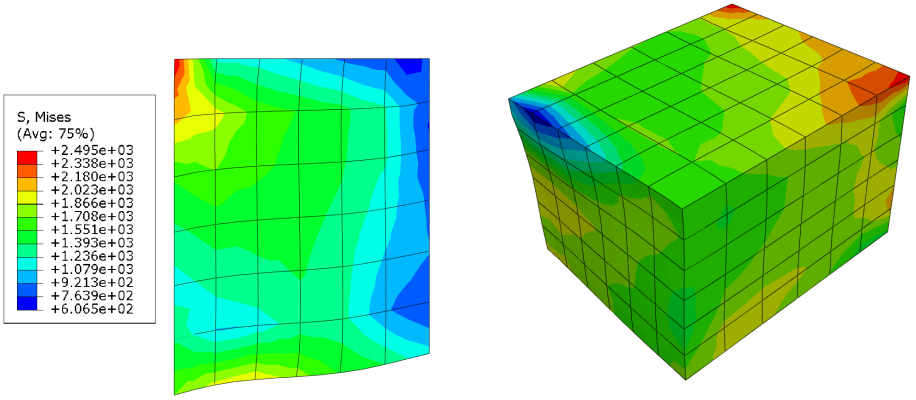

FIGURE 4.14: Planar view of the grain which has orientation 1; top view at left, isometric view at right

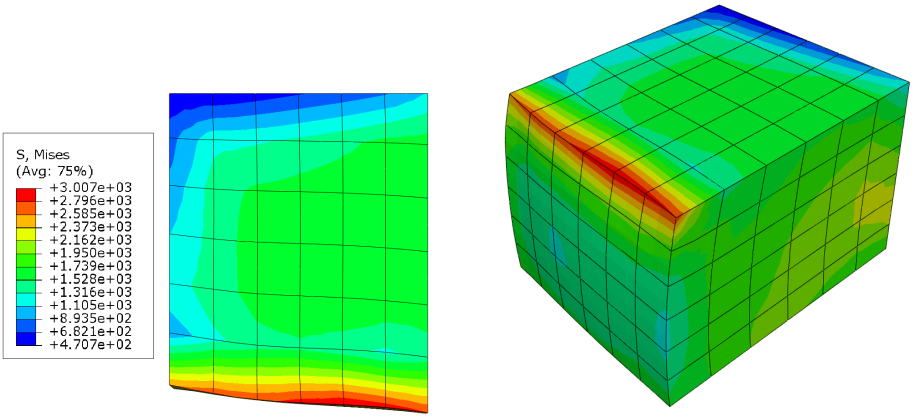

FIGURE 4.15: Planar view of the grain which has orientation 3; top view at left, isometric view at right

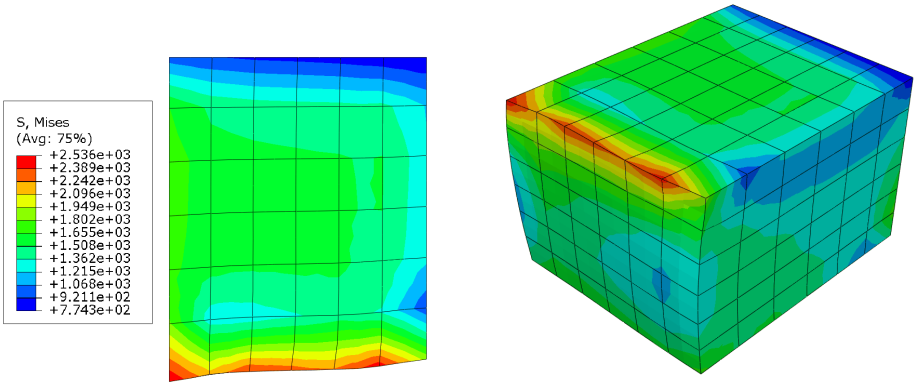

FIGURE 4.16: Planar view of the grain which has orientation 4; top view at left, isometric view at right

To investigate the effect of the grain orientation on friction, the ratio of the horizontal force acting on the top plate and vertical force acting on the top plate; which can be considered as the "macroscopic friction coefficient", has been plotted as a function of the vertical displacement imposed on the top plate, in figure 4.17.

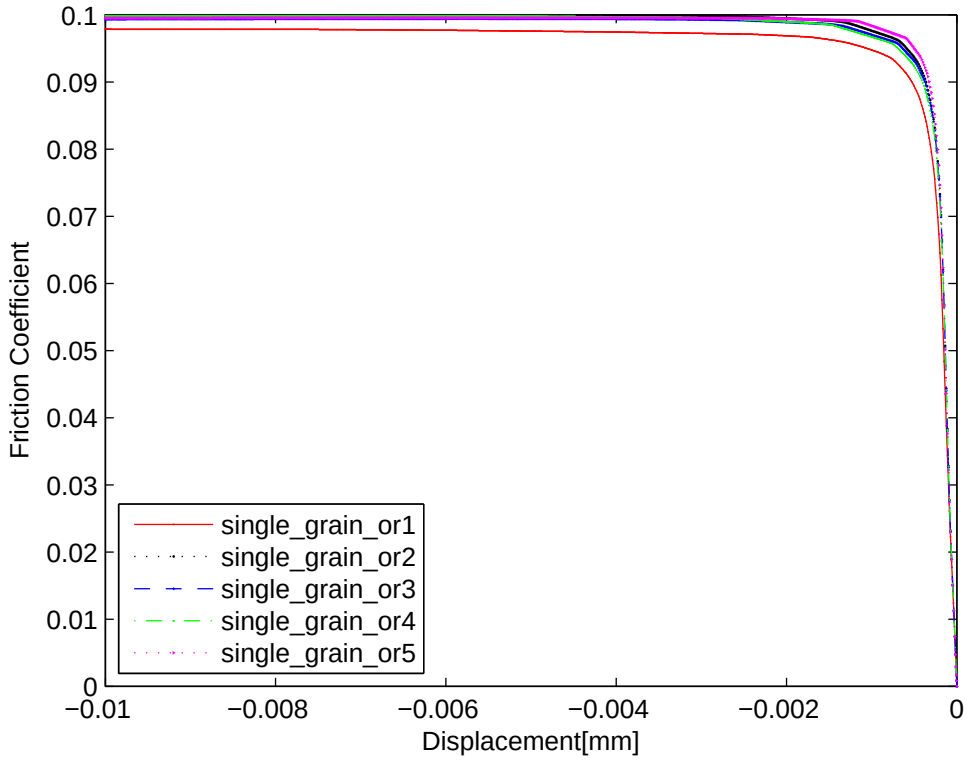

FIGURE 4.17: μ vs displacement for single grain orientations

These result indicate that after an initial sticking phase, the sliding starts almost at the same level of vertical displacement of the top plate. It is interesting to note that the macroscopic friction coefficient does not converge to exactly 0.1 for certain orientation sets. Furthermore there is non-negligible amount of scatter in the results.

To investigate the effect of hardening moduli on the evolution of the "macroscopic friction coefficient", an additional analysis with $h = 1.0MPa$ is conducted and compared with the case of $h = 40MPa$. These results are almost identical as shown in figure 4.18. Therefore the differences seen in figure 4.17 can be solely attributed to different grain orientations.

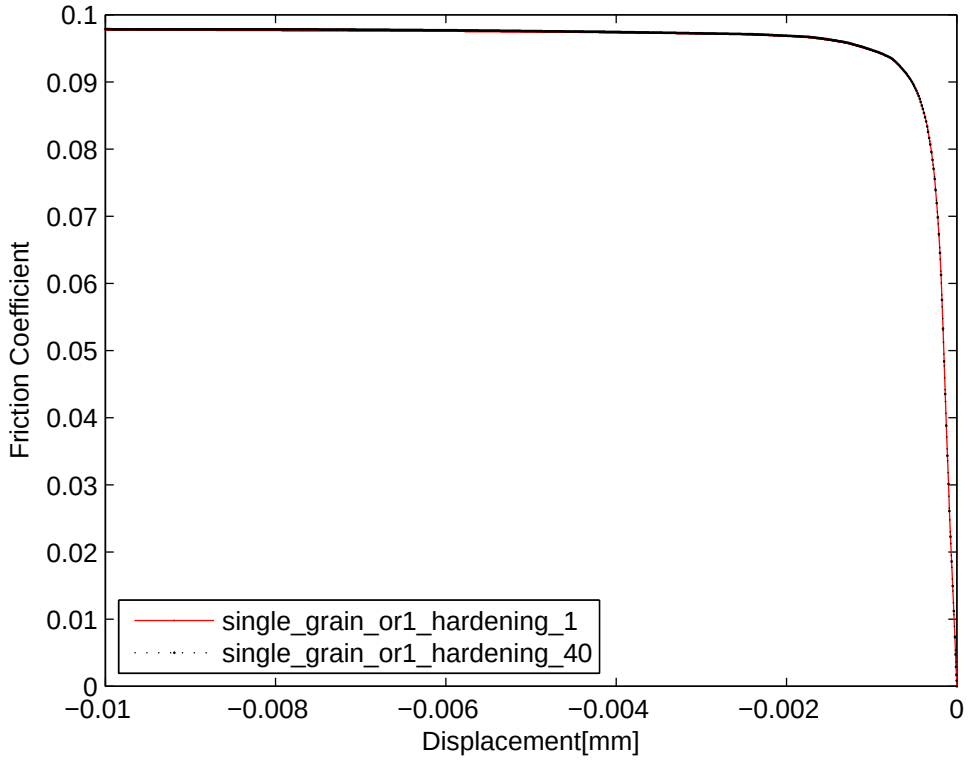

FIGURE 4.18: The influence of hardening parameter on macroscopic friction coefficient.

4.4.3 Case 2: Upsetting of Multiple-Grain Assemblies

In order to investigate the assembly behaviour of grains during micro-extrusion, the model presented in case 1 is expanded in terms of grains involved in the process. First, an assembly of five grains is considered with for five different sets of grain orientations, see table 4.3. In figure 4.19 the typical deformed configuration can be seen.

Five Grain		Grain1	Grain2	Grain3	Grain4	Grain5
Orientation 1	φ_1	229	344	86	243	104
	ϕ	62	140	121	1	108
	φ_2	116	282	169	12	63
Orientation 2	φ_1	87	330	96	275	67
	ϕ	116	122	114	170	37
	φ_2	114	42	338	232	172
Orientation 3	φ_1	114	42	338	232	172
	ϕ	39	19	19	11	72
	φ_2	69	49	250	33	189
Orientation 4	φ_1	293	326	45	328	227
	ϕ	17	50	98	172	173
	φ_2	56	349	344	174	288
Orientation 5	φ_1	51	151	329	285	345
	ϕ	118	6	152	168	122
	φ_2	272	267	141	235	61

TABLE 4.3: Euler Angles (given in degrees) used in five grain analysis

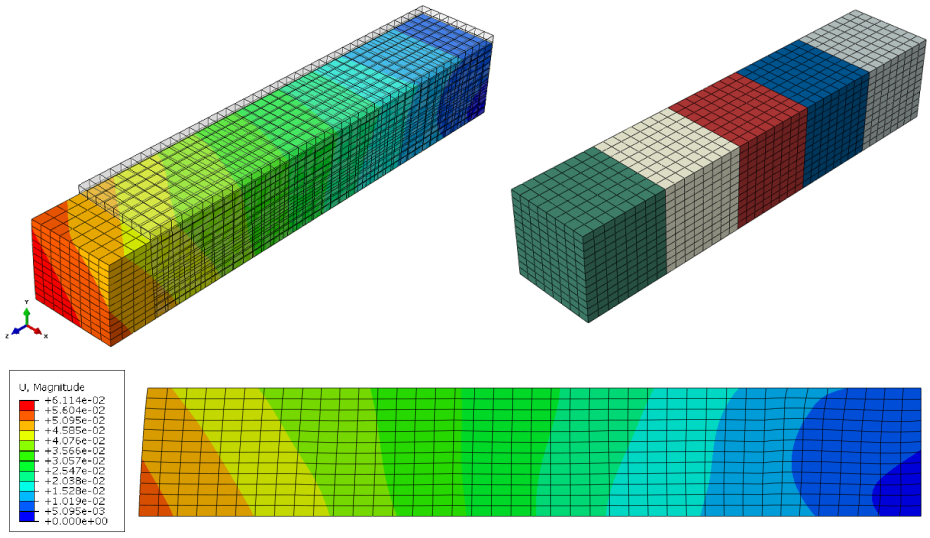

FIGURE 4.19: Deformed and undeformed states for the 5 grain assembly

To reflect the influence of grain orientations on local quantities, the slip in Z direction for two different orientations and the solution obtained by conventional plasticity model ($J2\,plasticity$) are presented in figure 4.20. The grain orientation leads to a non-uniform distribution of slip as compared to the conventional case. A similar result in terms of contact pressure along the center line of the top surface is shown in figure 4.21

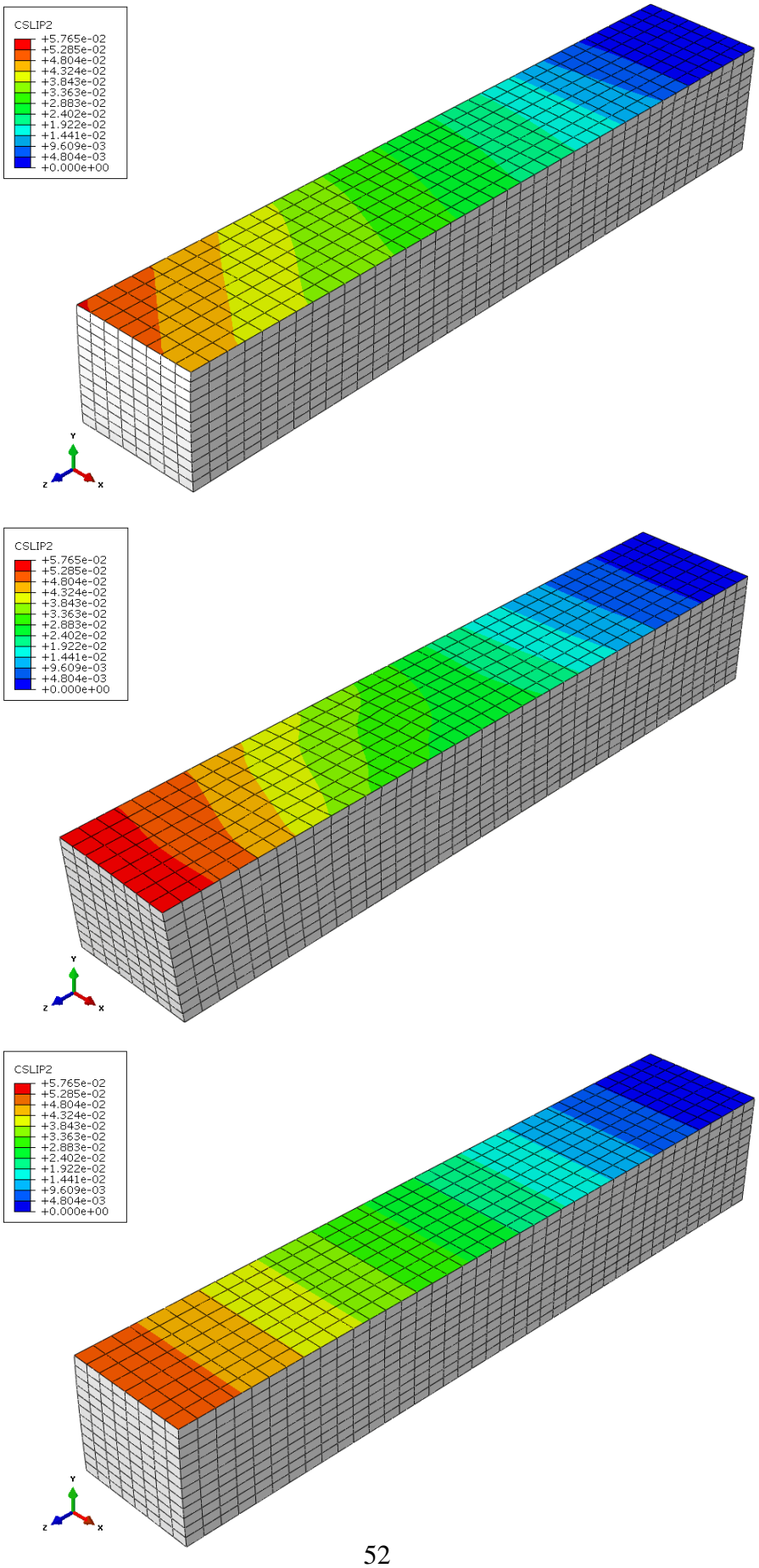

FIGURE 4.20: Slip distribution depending on different orientation and conventional method

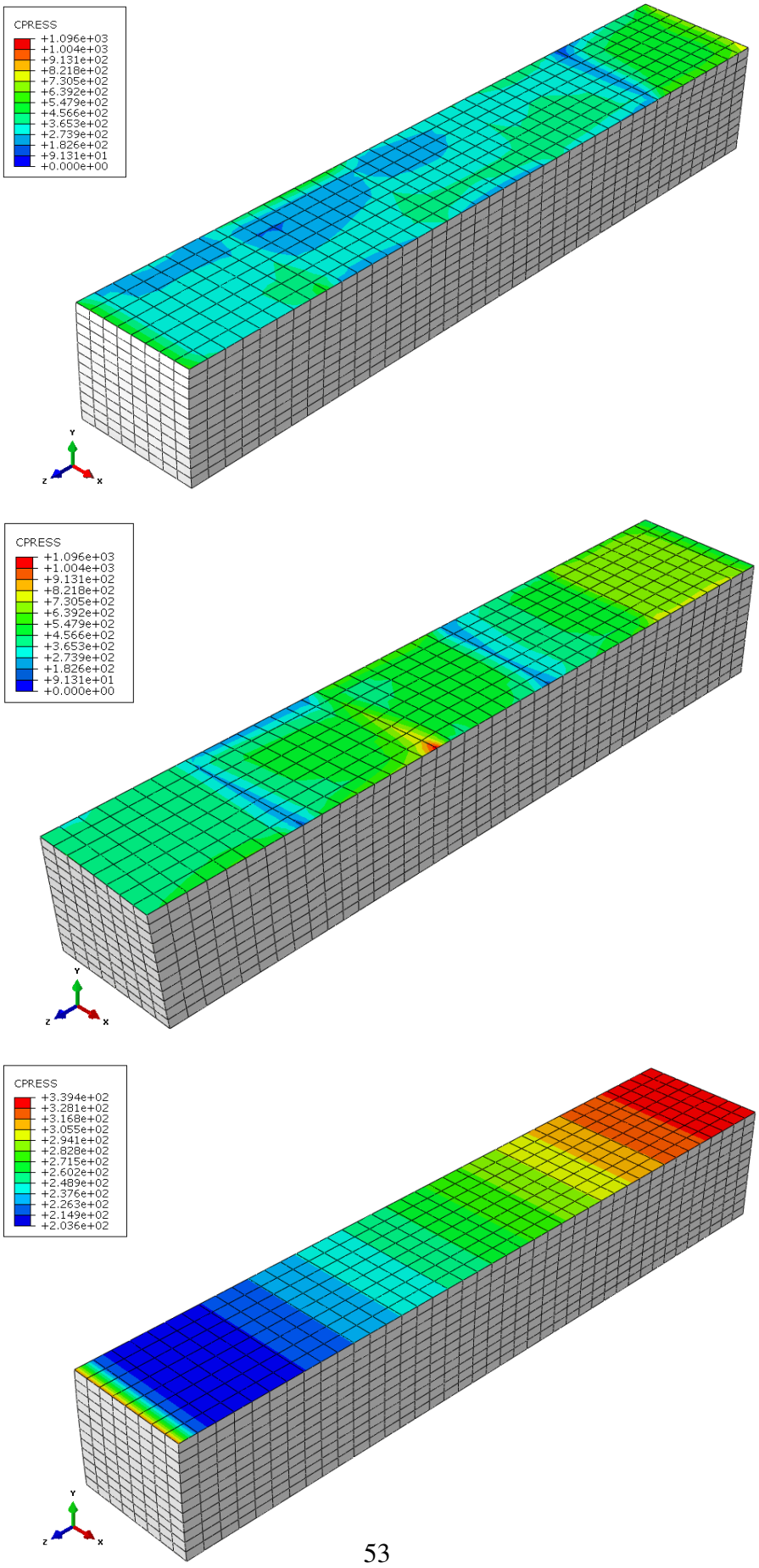

FIGURE 4.21: Normal pressure distribution depending on different orientation and conventional method

Quantitatively the pressure distributions are significantly different and the effect of grain boundaries, where the orientation changes, can be seen in the form of peaks and dips in figure 4.22 . The solution with J2 plasticity is far more uniform as seen in the same figure.

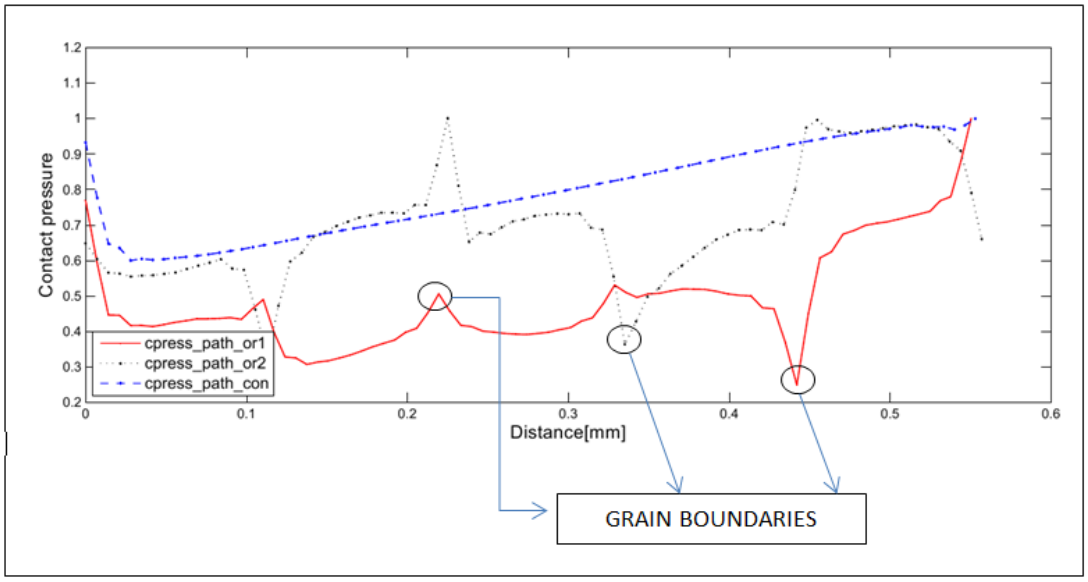

FIGURE 4.22: Normal Pressure distribution indicated on the grain boundries

Similar to the single grain case, the "macroscopic friction coefficient" evolution graphs are given in figure 4.23. The results are similar to the ones obtained from single grain analysis. A quantitative comparison is going to be given at the end of this chapter. Furthermore, to question the results obtained for single grain case for hardening parameter, an additional analysis with $h = 1MPa$ is conducted and the results are shown in figure 4.24. These results confirm that the hardening parameter does not lead to the scatter seen in the graphs in case of multiple grain assemblies.

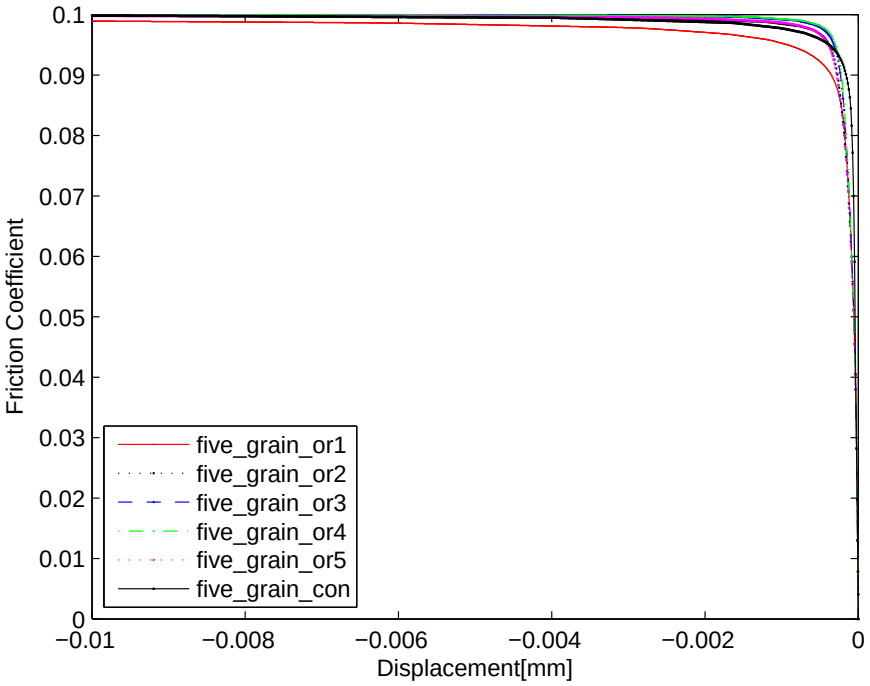

FIGURE 4.23: μ vs displacement for ten grain orientations

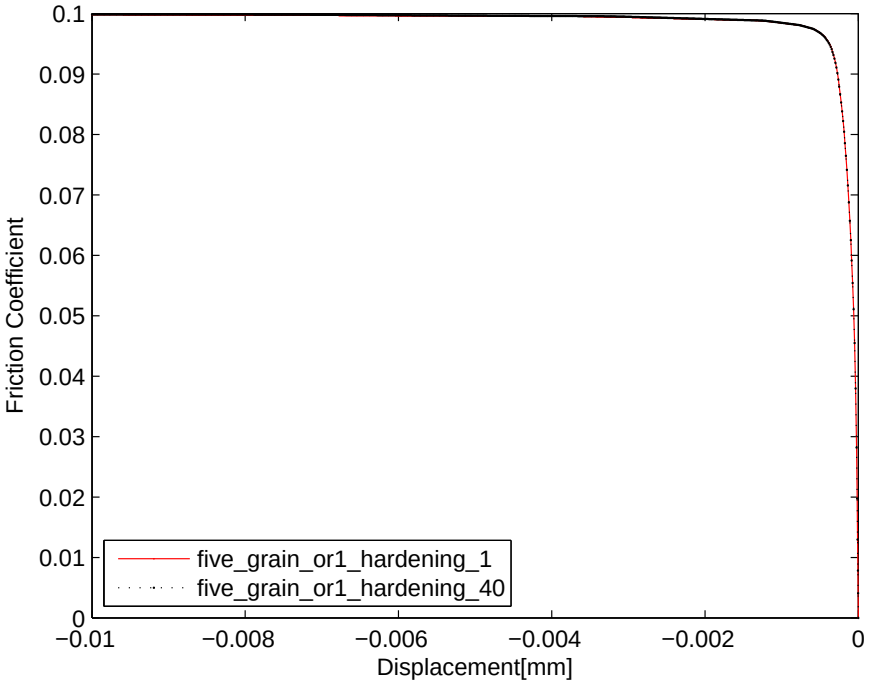

FIGURE 4.24: The influence of hardening parameter on macroscopic friction coefficient.

In order to see the influence of the number of grains, another model with ten grains (*see table* 4.4) have been constructed and similar analysis have been conducted. The deformed configuration at the end of the process is shown in figure 4.25. The non-homogeneous deformation mode is clearly present which can also be traced typically at the grain boundaries.

Similar to the previous cases, the "macroscopic friction coefficient" curves are given in figure 4.26. To investigate the effect of number of grains on friction coefficient, in figure 4.27, the difference between the maximum and minimum friction coefficients at certain vertical displacement values are plotted for different cases. In other words, the Y-axis of figure 4.27 can be considered as the measure of scatter in "macroscopic friction coefficient" . It can be seen that, once the plateau of the curves are reached, which corresponds to displacement levels of $4 \sim 5.10^{-3}$mm, the scatter diminishes as the number of grains increases.

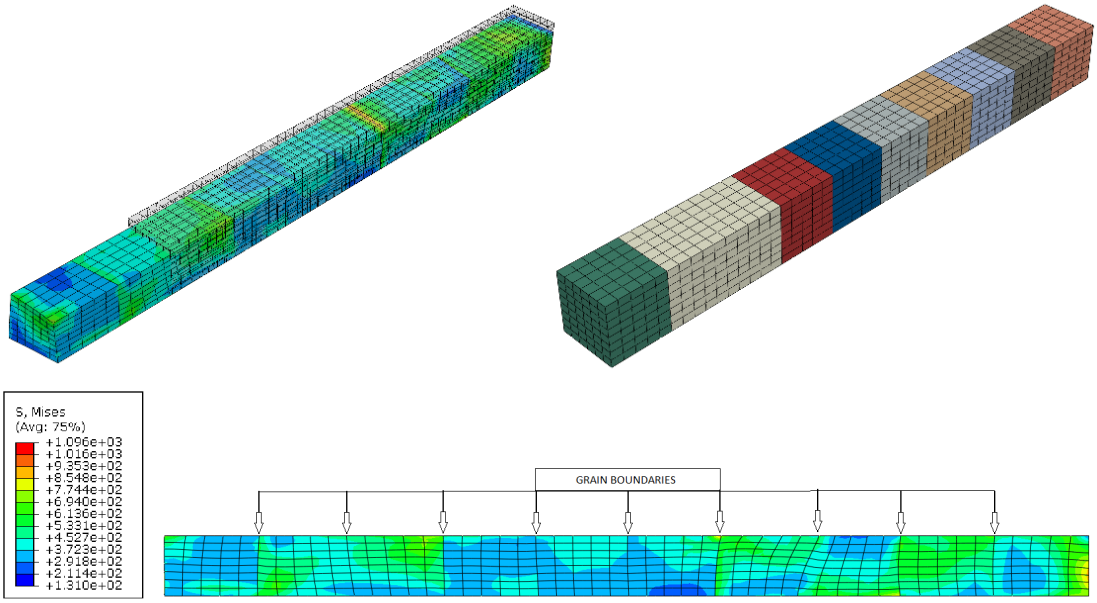

FIGURE 4.25: Deformed and undeformed states for the ten grain assembly

Ten Grain		Grain1	Grain2	Grain3	Grain4	Grain5
Orientation 1	φ_1	150	17	324	340	176
	ϕ	140	70	43	72	17
	φ_2	84	127	295	5	15
Orientation 2	φ_1	196	106	268	68	247
	ϕ	167	139	87	78	80
	φ_2	231	136	292	191	126
Orientation 3	φ_1	74	108	169	82	303
	ϕ	55	166	77	33	162
	φ_2	214	94	217	256	79
Orientation 4	φ_1	99	244	235	58	42
	ϕ	135	45	91	125	160
	φ_2	302	91	293	87	334
Orientation 5	φ_1	126	299	210	197	330
	ϕ	13	9	95	140	168
	φ_2	58	285	112	190	59
Ten Grain		Grain6	Grain7	Grain8	Grain9	Grain10
Orientation 1	φ_1	176	121	324	132	40
	ϕ	23	169	172	103	10
	φ_2	60	233	263	233	162
Orientation 2	φ_1	66	132	225	280	29
	ϕ	55	91	91	147	143
	φ_2	338	315	198	224	211
Orientation 3	φ_1	70	81	61	81	156
	ϕ	176	78	20	46	73
	φ_2	42	106	114	152	182
Orientation 4	φ_1	179	345	122	210	80
	ϕ	172	98	24	26	46
	φ_2	125	70	90	221	170
Orientation 5	φ_1	102	272	271	136	204
	ϕ	23	102	84	2	60
	φ_2	216	94	235	248	269

TABLE 4.4: Euler Angles (given in degrees) used in ten grain analysis

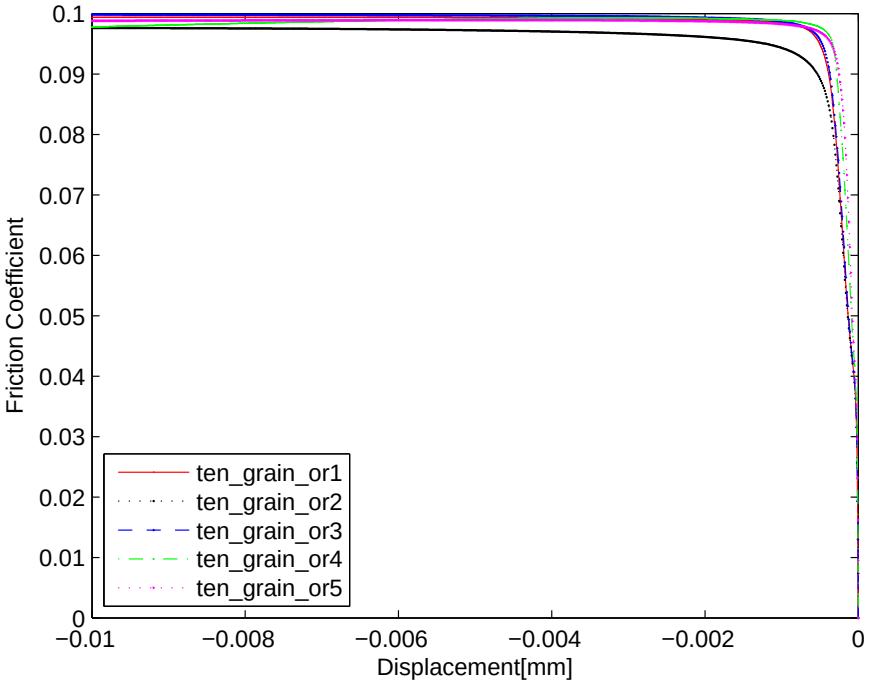

FIGURE 4.26: μ vs displacement for ten grain orientations

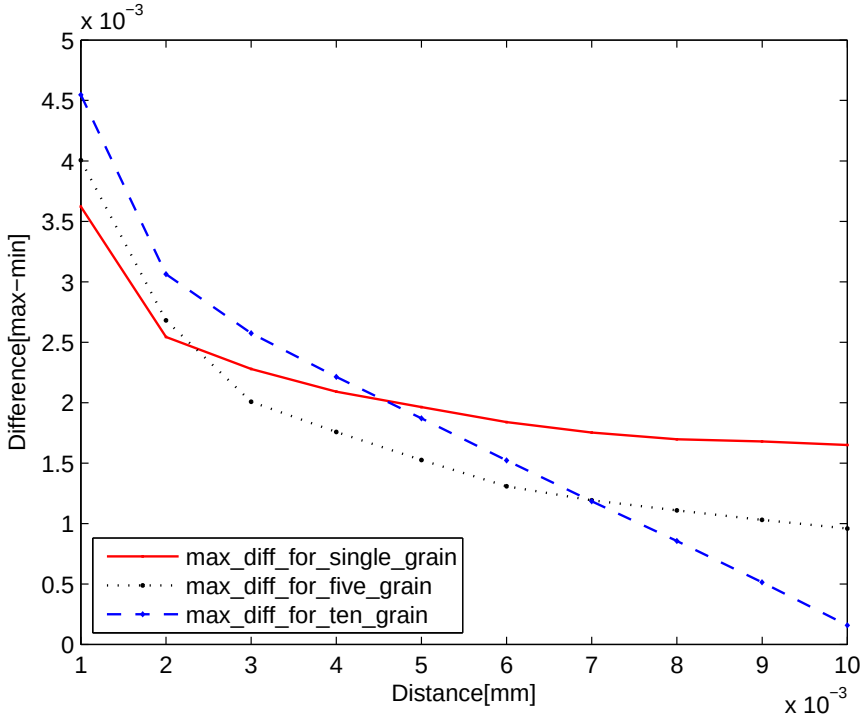

FIGURE 4.27: The scatter of μ for single, five and ten grains

CHAPTER 5

CONCLUSION AND OUTLOOK

Developing a proper understanding on micro-forming processes requires appropriate experimental set-ups and numerical tools. In this work, on the basis of these needs, a combined experimental-numerical investigation on micro-extrusion is presented.

On the experimental side, a set of extrusion dies have been designed and micro-extrusion experiments have been conducted successfully. Due to inherent anisotropic nature of the material and frictional behaviour, it is not appropriate to expect reproducible experimental results as exemplified by the force-displacement curves given in chapter 4. It is important to point out that the relatively large scatter is due to the combined influence of different bulk behaviour and non-similar tribological behaviour due to the uneven oxide layer developing on the specimens. Therefore this issue calls for further experimental studies possibly with billets which were heat treated under vacuum since such treatment conditions prevent the formation of oxide layer.

Furthermore, the experimental studies can be enriched by using smaller billet diameters and different cross-sectional reductions during micro-extrusion. In fact, such die and billet geometries were also used in this work but extrusion process could not be realized due to limitation on the capacity of the punch and the lack of a dedicated press for the micro-extrusion process.

On the modelling side, the appropriate framework namely the crystal plasticity model is integrated into the commercial FE software Abaqus as a user defined material routine (UMAT) and a set of numerical experiments were conducted. To gain a better understanding and exclude some of the geometric parameters, relatively simple models in terms of geometry are used intentionally. Starting from single grain models, the influence of grain orientation and boundary conditions on the frictional response have been

investigated. The numerical results clearly demonstrates the influence of the grain orientation and different frictional response stemming from the bulk behaviour, although an identical friction model was used. These results suggest that, especially in case of friction characterization at small scales, it might be necessary to take into account the grain level information in the modelling process since typically an inverse technique is used to determine the coefficient of friction using the experimental force-displacement curves. Furthermore, as the number of grains increases, the limiting behaviour should be an isotropic one, which is to a certain extend demonstrated by the numerical tests on assemblies of different grain numbers.

There are numerous of improvements that have to be incorporated in future studies. First of all, the influence of other material parameters have not been addressed in this work. This could be done relatively easily with the developed modelling framework. Probably, before that, the phenomenological hardening model should be replaced with a physically motivated one which is based on defect densities and their evolution. Furthermore, the multiple-grain models require appropriate description for the grain boundaries, which is an active research topic on its own. A similar issue is the incorporation of the physical size effect which requires higher order descriptions (strain-gradient theories) and closely linked with the hardening models that take into account the evolution of defects, e.g. dislocations. The study can be further enriched by using realistic grain level geometric models obtained either from real micro-structural data or artificially generated using Voronoi diagrams or other techniques. However the presented model and its implementation can be readily used as the backbone of these future studies not only in the context of micro-extrusion but also for the modelling of other micro-forming processes and characterization tests such as the flaring tests on micro-tubes [23].

BIBLIOGRAPHY

[1] U.Engel, R. Eckstein. Microforming - From basic research to its realization. Journal of Material Processing and Technology, 125-126,3544[2002]

[2] www.deltacomposants.com

[3] A.Meisnerr, M. Geiger, U. Engel. Size effect on the FE-simulation of microforming process, J Mater.Process. Tehcnol.45, 371-376,[1994]

[4] J.Stolken, A.Evans. A microbend test method to measuring the plasticity length scale, Acta Materialia, 46, 5109-5115 [1998]

[5] N. Krishnan, J. Cao, K. Dohda. Study of size effect and friction condition in microextrusion-Part 2: Size effect in dynamic friction for brass-steel pairs.Journal of Manufacturing Science and Engineering, vol. : 129 [2007]

[6] F.Vollorsten, Z.Hu, H.Schulze, C. Niehf, C. Theiler. State of the art in micro forming and investigations into micro deep drawing, Journal of Materials Processing Technology 151, 70-79[2004]

[7] M. Geiger, U. Engel, F. Vollertsen, R. Kals, A. Mebner, Metal forming of Micro parts for electronics. Production Engineering, vol: II/1, 15-18, [1994]

[8] W. Wang ,W., R.H. Wagoner, X. J. Wang, Measurement of friction under the sheet forming condition. Metall. Mater. Trans. A. , 27(12), 3971-3981, [1996]

[9] J.P. Davim. An Experimental study on the tribological behaviour of the brass/steel.J. Mater. Process. Technol., 100(1-3),273-277, [2000]

[10] D.E. Kim, D.H. Hwang. Experimental investigation of the influence of the machining condition on the contact sliding behaviour of the Metals. ASME J. Manuf. Sci. Eng. , 120(2), 395-400, [1998]

[11] E. Egerer, U. Engel. Process Characterization and material flow in micro forming at elevated temperature. Journal of Manufacturing Processes, vol:6/1, [2004]

[12] N.Teisler, U. Engel, M.Geiger. Forming of Micro part-Effect of miniaturization on friction. Proceedings of the Sixth ITCP,vol.2, 889-894,[1999]

[13] J. Cao, N. Krishnan, Z. Wang, H. Lu, W.K. Liu, A.Swanson. Experimental investigation of extrusion process for micro-pin and its numerical simulation using RKEM. Transaction of the ASME, vol.126,[2004]

[14] R. Eckstein, M. Geiger, U. Engel. Specific Characteristics of Micro Sheet Metal forming.Proceeding of SheMet. , 529-536, [1999]

[15] S. GeiBdörfer, U. Engel, M. Geiger. Mesoscopic model-Simulative approach to the scatter of the process factors in micro-forming. 1^{st} Colloguium Processscaling, Bremen, 28./29.10.[2003]

[16] D. Peirce, R.J. Asaro, A Needleman. An analysis of non-uniform and localized deformation in ductile single crystals. Acta Metallurgica 30(6), 1087-1119, [1983]

[17] G. Sarma, B. Radhakrishnan, P. Dawson. Mesoscale Modelling of Microstructure and Texture Evaluation During Deformation Processing of The Material. Advanced Engineering Materials, 2002(4)7, 509-514, [2002]

[18] E.A. de Souza Neto, D. Peric, D.R.J. Owen. Computational Methods For Plasticity Theory and Applications, Wiley [2008]

[19] P. Wriggers. Computational Contact Mechanics.2^{nd} Edition,Springer [2006]

[20] J. Bonet, R.D. Wood. Non-linear Continuum Mechanics For Finite Element Analysis.2^{nd} Edition, Cambridge [2008]

[21] Jr. W.D. Callister, D.G. Rethwisch. Material Science and Engineering An Introduction. 8^{th} Edition, Wiley [2009]

[22] R. Quey. Orientation Library Version 1.1 [2008], www.sourceforge.net/projects/orilib

[23] M.A. Mirza, K. Manabe, T. Mabuchi. Deformation characteristics of microtubes in flaring test. Journal of Materials Processing Technology, 201(2008), 214-219, [2008]